ARL

US Army Research Laboratory

Processing and Characterization of Lightweight Syntactic Materials

by Oliver Strbik III and Vincent H Hammond

NOTICES

Disclaimers

ARL

US Army Research Laboratory

Processing and Characterization of Lightweight Syntactic Materials

by Oliver Strbik III
Deep Springs Technology, LLC, Toledo, Ohio

by Vincent H Hammond
Weapons and Materials Research Directorate, ARL

REPORT DOCUMENTATION PAGE

1. REPORT DATE *(DD-MM-YYYY)*	2. REPORT TYPE	3. DATES COVERED (From - To)
October 2016	Technical Report	July 2010–November 2015

4. TITLE AND SUBTITLE	5a. CONTRACT NUMBER
Processing and Characterization of Lightweight Syntactic Materials	W911NF-10-2-008
	5b. GRANT NUMBER
	5c. PROGRAM ELEMENT NUMBER

6. AUTHOR(S)	5d. PROJECT NUMBER
Oliver Strbik III and Vincent H Hammond	
	5e. TASK NUMBER
	5f. WORK UNIT NUMBER

7. PERFORMING ORGANIZATION NAME(S) AND ADDRESS(ES)	8. PERFORMING ORGANIZATION REPORT NUMBER
US Army Research Laboratory ATTN: RDRL-WMM-F Aberdeen Proving Ground, MD 21005-5069	ARL-TR-7857

9. SPONSORING/MONITORING AGENCY NAME(S) AND ADDRESS(ES)	10. SPONSOR/MONITOR'S ACRONYM(S)
	11. SPONSOR/MONITOR'S REPORT NUMBER(S)

12. DISTRIBUTION/AVAILABILITY STATEMENT

Approved for public release; distribution is unlimited.

13. SUPPLEMENTARY NOTES

14. ABSTRACT

Composed of hollow spheres encapsulated in a metal matrix, syntactic metal foams offer significant potential as lightweight energy-absorbing materials. Moreover, due to the ability to select shell composition and shape, as well as matrix materials, these materials can readily be optimized for a given application and/or property requirement (density, compressive strength, etc.) This report details the noteworthy advances achieved in the processing and characterization of hollow spheres as well as their subsequent incorporation into lightweight (aluminum, magnesium) metal matrices via various metal processing methods. The performance of the resulting foam materials under quasi-static and dynamic loading, as well as their thermal and acoustic response, are presented and discussed. In addition, the performance of armor packages that incorporate selected syntactic metal foams against representative threats was evaluated in comparison with current standards. Collectively, results from the various studies indicate that syntactic metal foams can offer significant advantages in performance accompanied by appreciable weight savings. Consequently, it is anticipated that syntactic metal foams will soon be considered for a range of applications in various industrial sectors (automotive, aerospace, etc.).

15. SUBJECT TERMS

hollow spheres, syntactic metal foams, processing, mechanical properties, ballistic properties

16. SECURITY CLASSIFICATION OF:			17. LIMITATION OF ABSTRACT	18. NUMBER OF PAGES	19a. NAME OF RESPONSIBLE PERSON
					Vincent H Hammond
a. REPORT	b. ABSTRACT	c. THIS PAGE	UU	82	19b. TELEPHONE NUMBER (Include area code)
Unclassified	Unclassified	Unclassified			410-278-2752

Contents

List of Figures

List of Tables

1.   Introduction

Conventional composite materials, in which a matrix material is reinforced by particulates, whiskers, and/or continuous fibers, have long been of interest as potential materials solutions to engineering needs. Typically, the benefits of these reinforcements are observed for cases of tensile loading, with only minimal improvement for cases of compressive loading (e.g., "you can't push on a rope"). As a result, recent attention has grown in the use of hollow spheres as a potential reinforcement in metallic systems. Commonly known as syntactic foams, the hollow spheres display a prolonged region under compressive loading in which the spheres deform by crushing, thereby absorbing a large amount of deformation energy. Furthermore, as an added benefit, the inclusion of hollow spheres also serves to lower the weight of the final component, thereby offering the possibility of improved performance with a simultaneous reduction in system weight. Thus, these materials are primarily being considered for applications that require a high capacity for absorbing energy (bumpers, struts, etc.).

When subjected to a compressive load, the hollow spheres (as well as composites based on these materials) typically display a characteristic stress-strain relationship with 4 main areas, as seen in Fig. 1. After an initial region characterized by a linear-elastic response (i), the cellular materials experience buckling, plastic deformation and collapse of intercellular walls as they enter the transition zone (ii). Under further loading, the mechanism of buckling and collapse becomes even more pronounced, which is manifested in large strains at almost constant stress (iii). The stress level σ_{pl} indicates the beginning of this plateau region in which the gradient of stress plateau is denoted as plateau modulus P. Cellular structure densification is observed after reaching some critical strain σ_d, and the stress level increases exponentially thereafter (iv). The cellular material is able to absorb a significant amount of impact energy through its elastic and plastic deformation during the loading process, as represented by the area under the strain-stress curve.
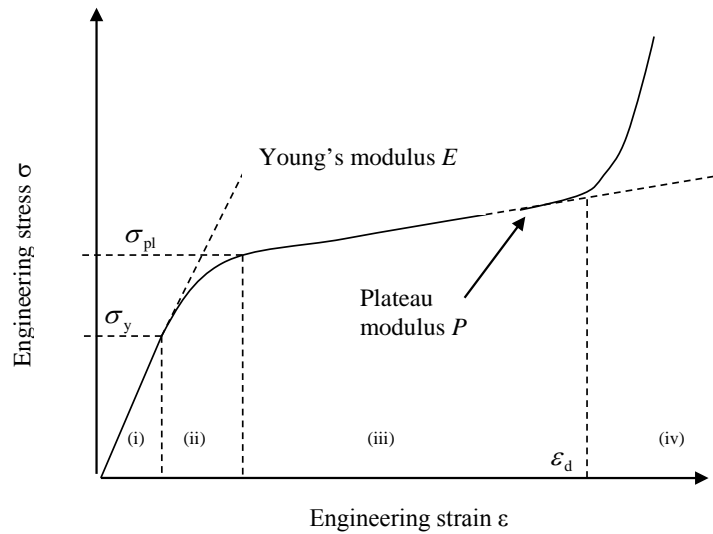
Fig. 1   Schematic drawing of the stress-strain behavior of porous materials under impact loading

Most of the early research in metal syntactic foams has focused on the use of fly ash spheres that were produced as a by-product of fuel combustion. Although composites reinforced with such materials showed improved energy absorption capabilities, the manner in which these spheres are produced resulted in a large (and mostly random) distribution of size, geometry, and composition. This inherent variability in ash-based spheres made it practically impossible to produce repeatable foams over a long processing time frame. As such, definitive conclusions regarding the influence of sphere parameters on performance could not be reached.

More recently, a process has been developed that can produce hollow metal and/or ceramic spheres with consistent and repeatable properties. In this process, a suspension of metal and/or ceramic powder is sprayed onto a polymer support (e.g., spheres) to form a green body that is then sintered to produce the final sphere material. As can be envisioned, the ability to tailor the process (suspension composition, coating time, etc.) directly translates into the ability to produce spheres with customized—and repeatable—compositions and/or geometries. This, in turn, allows one to create composite materials specifically designed for a given application.

In a project designed to evaluate the potential of such materials for use in Army-relevant applications, the US Army Research Laboratory entered into a collaborative effort with Deep Springs Technology (DST) (Toledo, Ohio). The focus of this joint effort was to identify and develop processing method(s) for incorporating the hollow spheres into a light metal (aluminum [Al], magnesium [Mg]) alloy matrix. Several mechanical and physical tests were then used to

determine the performance of the resulting hollow metal sphere composites. Furthermore, a series of more specialized tests was performed on a limited number of composite samples. The highlights of this research effort are detailed in this report.

2. Hollow Spheres: Development, Processing, and Testing

As detailed in the introduction, hollow spheres and their composites typically display a region of steady state deformation in which significant amounts of energy can be absorbed when subjected to compressive loading. The reason for this behavior can readily be seen in Fig. 2, which visually documents the extensive deformation of a M350 maraging steel hollow sphere. However, in contrast, ceramic spheres (silicon carbide [SiC], aluminum oxide [Al_2O_3], etc.) typically possess high yield strengths that require the application of significant stresses to achieve fracture. For both classes, important parameters that dictate the material response include wall thickness, composition, grain size, and porosity (both type and location).

Fig. 2   Deformation of compressed M350 hollow sphere into right circular cylinders

2.1 Structure

Each syntactic foam application will require the engineered hollow particle to exhibit specific properties to meet the performance requirements. Hollow particles can be classified by their geometry and composition (e.g., SiC, Al_2O_3), which contribute to significant performance properties such as density and strength of the syntactic. Chemical composition of the hollow particle will be an important factor during the design process for both fabrication and application considerations.

2.1.1 Geometry

Initial efforts by DST resulted in the development of the ability to produce spherical shells in a broad range of sizes and compositions (Fig. 3). As an extension of their approach to producing hollow spheres, DST has used the method to produce a variety of additional hollow shapes. As seen in Fig. 4, discs, triangles, and

rectangular prisms of various dimensions can be produced. The ability to produce a range of such diverse shapes will allow DST to further tailor the design of syntactic foams to the requirements of a particular application.
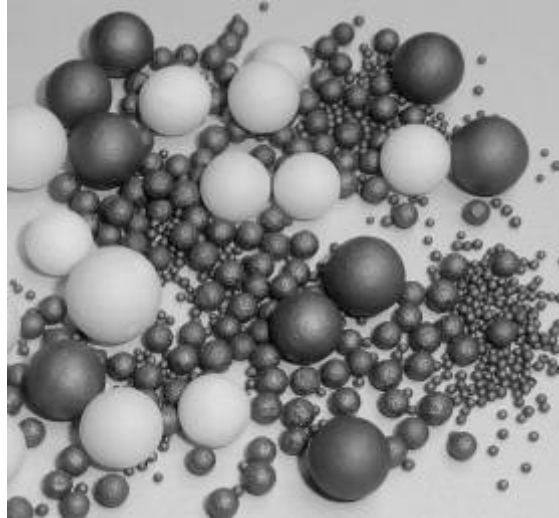
Fig. 3   Spherical hollow shells

Fig. 4   The variety of hollow shapes that can be produced by DST using their expendable hollow core processing method

2.1.2 Aspect Ratio

The aspect ratio for a hollow sphere is determined by the ratio of the outer diameter (D_o) to the average wall thickness (t_{avg})

$$a = D_o / t_{avg} \tag{1}$$

and is usually expressed as

$$D_o : t_{avg} . \tag{2}$$

The aspect ratio is dependent upon the method of manufacture as well as the material selected. Shells currently in production have aspect ratios ranging from 15:1 to 60:1. The hollow shell shown in Fig. 5 has a diameter of 6.5 mm and an average wall thickness of 0.175 mm resulting in a 37:1 aspect ratio.
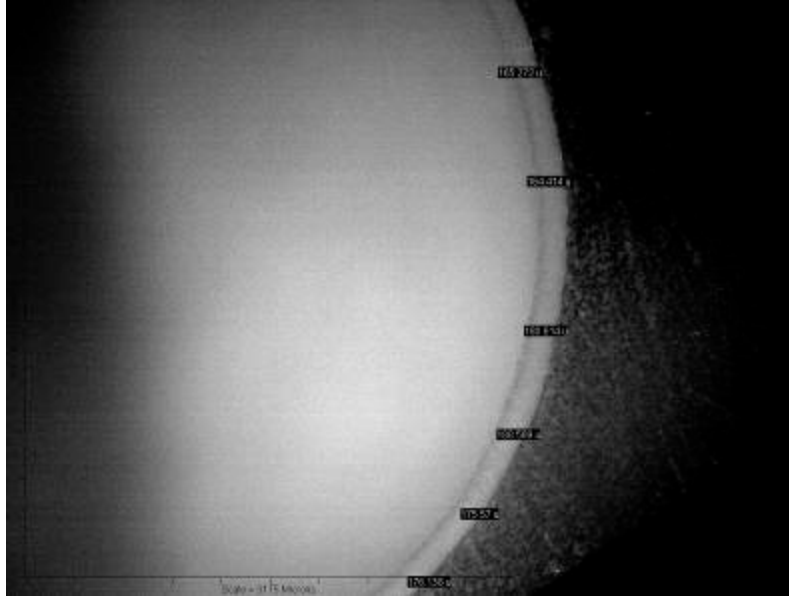
Fig. 5   Hollow alumina shell with 37:1 aspect ratio

2.1.3 Sphericity

Hollow particles will deviate from a perfect sphere due to manufacturing techniques and subsequent heat treatment or cooling during processing. When collapse strength is important, the maximum local radius of curvature is compared with the average radius of the sphere to determine sphericity (Fig. 6).

$$Sphericity = \frac{\text{Maximum local radius of curvature}}{\text{Average radius of sphere}} . \tag{3}$$
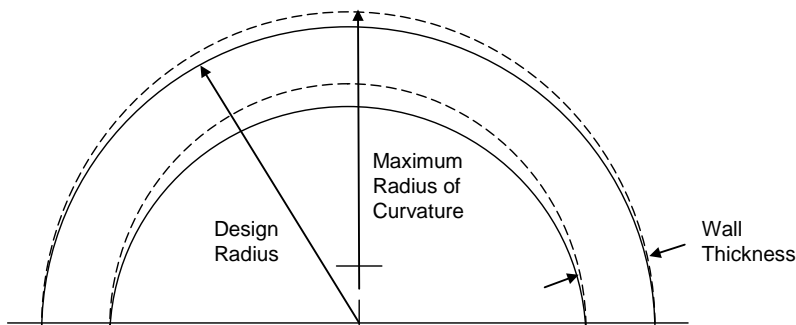
Fig. 6   Representation of hollow sphere parameters

The collapse strength of a sphere will not be critically affected by sphere radius that varies from the design radius if the deviation arc length is less than the critical arc length. The critical arc length L_C is defined by

$$L_C = 2.2(r_c \times t_c)^{1/2} / (3(1-v^2)/4)^{1/4} \quad (mm),\qquad (4)$$

where r_c is the local radius of curvature, t_c is the average wall thickness in this length, and v is the Poisson's ratio of the particle material.

2.1.4 Density

Hollow sphere density will directly affect the overall density of the metal matrix syntactic foam. For applications such as buoyancy (Fig. 7), the hollow sphere density and strength are critical in the final compressive strength of the syntactic foam. Two types of densities can be defined for hollow spheres:

- Bulk Density: The mass of the spheres divided by the volume they occupy that includes the space between the spheres (ASTM-D5004-11 2011).

- True Density (also called true sphere density): The mass of a sphere divided by its volume. For a hollow sphere the internal void will be included in the volume. Internal voids in the shell wall will also be included in the volume.

Fig. 7   Buoyancy module featuring SiC and glass hollow spheres in a bimodal distribution

Macro (diameters greater than 0.50 mm) hollow sphere density and wall thickness can be calculated from physical samples. For each sphere, mass (m) and average

diameter (d_{avg}) are measured, from which the sphere density (ρ_s) can be calculated using

$$\rho_s = \frac{m}{\frac{4}{3}\pi\left(\frac{d_{avg}}{2}\right)^3} \, .$$

(5)

From the sphere density and the density of the wall material (ρ_0), a relative density (f_v) for each sphere is determined by

$$f_v = \frac{\rho_s}{\rho_0} \, .$$

(6)

Wall thickness (t) can be calculated using the relative density and the average diameter by

$$t = \frac{(d_{avg}/2)f_v}{3} \, .$$

(7)

Figure 8 shows the cross section of a typical sphere with a relative density of 25%.
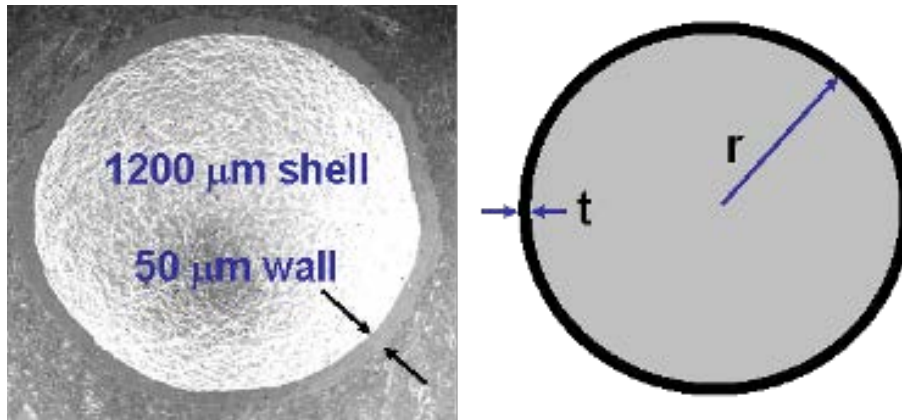
Fig. 8   Cross section of a typical hollow sphere with 25% relative density

2.2 Sphere Development

During this study, a series of hollow spheres of various compositions were produced. This section will briefly discuss some of the more important materials as well as the properties and/or performance of the associated hollow spheres. It is important to keep in mind that the materials used in the hollow spheres were selected based on compatibility with their intended matrices. Furthermore, although this report primarily focuses on ceramic-based spheres discussed, it is important to note that DST has produced a range of metallic spheres as well.

2.2.1 Silicon Carbide

Through funding obtained from the National Science Foundation, DST developed the processing knowledge and capability to consistently produce SiC spheres with a wall density of 3.15–3.18 g/cm^3 (theoretical density ~ 3.20 g/cm^3) in a broad range of diameters (Figs. 9 and 10). Subsequent analysis of the sphere walls indicated that the spheres were composed of stoichiometric SiC (Fig. 11). When subjected to compressive loading, the SiC spheres remained intact and undamaged after isotropic pressure loadings in excess of 415 MPa.
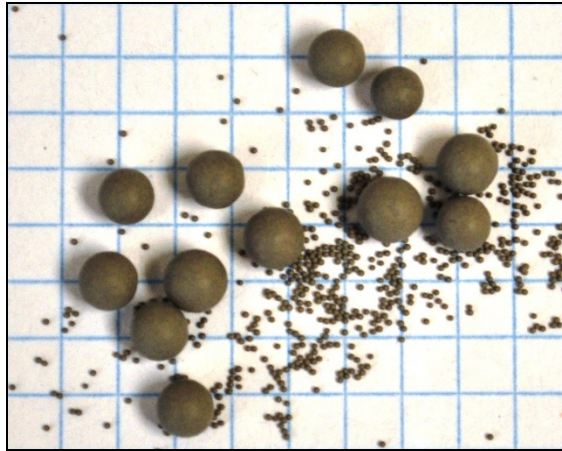
Fig. 9   Hollow SiC spheres were produced with diameters as small as 0.4 mm and larger than 5.9 mm

(a)	**(b)**
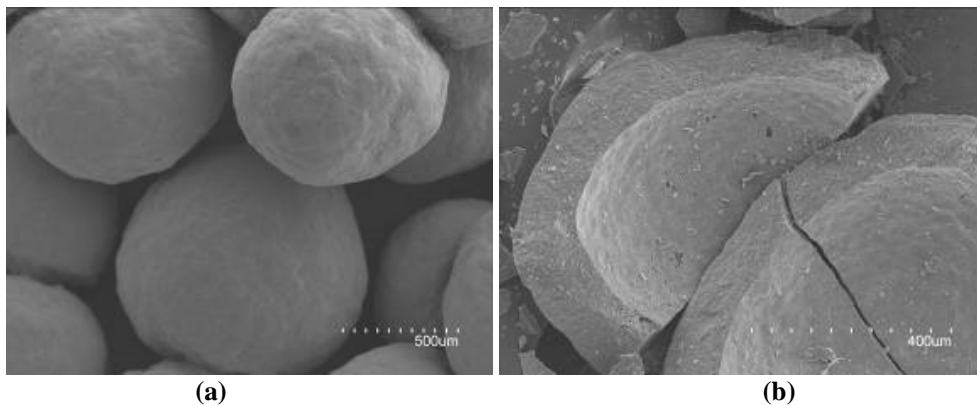
Fig. 10   a) Scanning electron micrograph (SEM) of a sample of SiC hollow spheres and b) wall thickness can be visualized in a broken particle
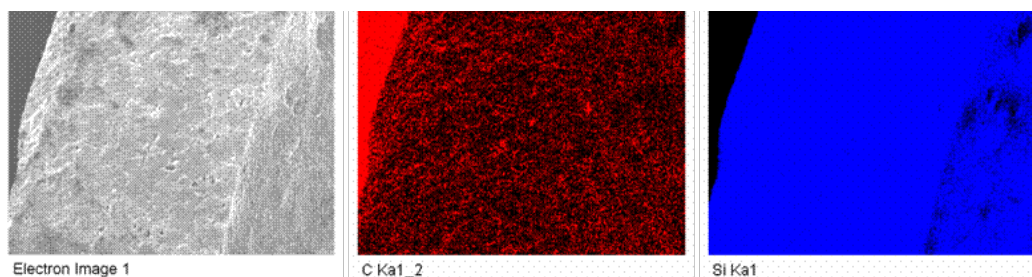
Fig. 11   Energy dispersive X-ray spectroscopy (EDS) map showing even distribution of elemental carbon (in red) and silicon (in blue). The electron image is of a hollow SiC sphere wall cross section mounted in carbon paste.

2.2.2   Boron Carbide (B₄C)

With an intent of producing extremely low-density hollow sphere metal composites, an effort was undertaken to produce B_4C spheres. In addition to a very low density for a ceramic material (2.52 g/cm^3), B_4C is also highly compatible with magnesium, the lightest metal currently being considered for engineering applications. Using the process outlined previously, "green" spheres were prepared and fired at either 2100 or 2200 °C. The resultant spheres had diameters of 2.5–3.5 mm, with a wall thickness of approximately 150 µm. The wall density was greater than 90% for spheres fired at 2100 °C and greater than 95% for those fired at 2200 °C. Based on these positive results, efforts have continued at the production, characterization, and utilization of B_4C spheres.

2.2.3   Aluminum Oxide (Al₂O₃)

The refinement of the manufacture of aluminum oxide hollow spheres was largely carried out under a National Institute of Standards and Technology Advanced Technology Program. The focus of the program was to fabricate a hermetic hollow sphere that was filled with an ionizable gas that could be excited with an electric field causing the gas to ignite into a plasma. These spheres could be used as pixels in a display application. Figure 12 shows a set of loose hollow discs excited on a radio frequency platform as a metal tweezer that acts as a ground as it passes over them. As the manufacturing process matured and grew in production capacity, the application for the alumina hollow spheres in structural applications became feasible. The process has grown from partial liters to cubic meters.

Fig. 12   Short hollow Al$_2$O$_3$ shells filled with an ionizable gas that has been ignited into a plasma due to presence of an electric field. The maturation of the production process for these shells has allowed their use in syntactic foams.

2.3 Hydrostatic Compression Testing of Spheres

A hydrostatic compression test fixture has been constructed and used to measure the compressive properties of the hollow spheres (Fig. 13) up to a maximum pressure of 140 MPa. Numerous compression tests have been performed to compare sphere materials and to determine if there is a correlation between strength and density. To test the spheres, each sphere is placed in the pressure vessel that is then filled with water and purged of air. Using a manual pressure generator, the system is pressurized to a predetermined pressure. When a sphere fails, there is a large pressure drop and an audible ping. The maximum pressure reached prior to failure is recorded.

Fig. 13 Hydrostatic compression tester

One example of the tests performed is the comparison of the response of SiC hollow spheres with a nominal diameter of 6.5 mm to that of alumina spheres of the same size. Multiple batches of spheres with varying densities were tested to 103 MPa. As shown in Figs. 14 and 15, there is, in general, a slight trend of increasing strength with increase in density. Failures were found to be random until the material reached a certain density. For silicon carbide this density was approximately 0.43 g/cm^3 true density. This density was significantly greater than the alumina spheres, in which failure did not occur once a true sphere density just under 0.30g/cm^3 was obtained. The randomness of the failures is assumed to be caused by surface defects, or thin sections in the wall of the sphere. This test setup is used on a regular basis to evaluate any processing-related changes on sphere performance and structure.
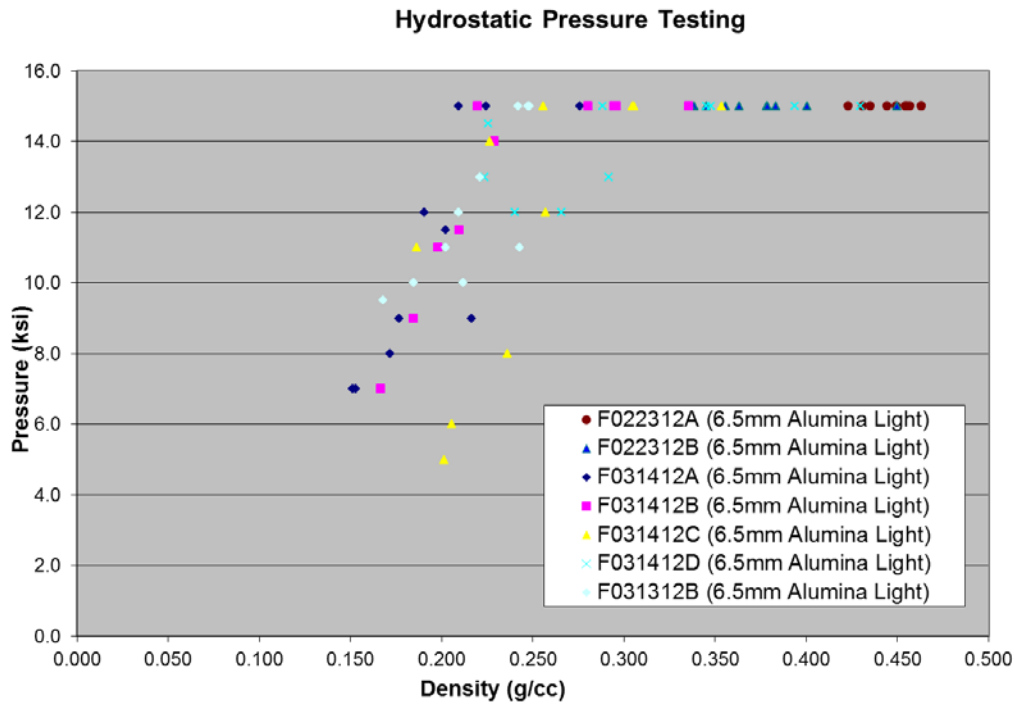
Fig. 14 Hydrostatic compression strength for alumina oxide 6.5-mm hollow spheres as a function of density
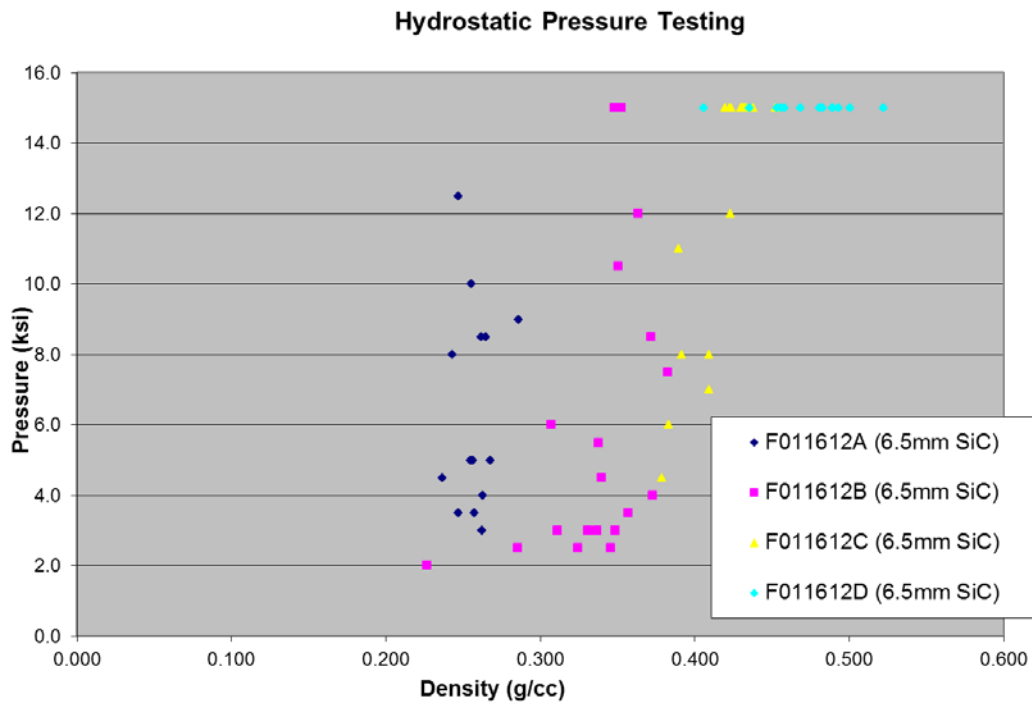
Fig. 15 Hydrostatic compression strength for SiC 6.5-mm hollow spheres as a function of density

12

3. Processing of Lightweight Syntactic Armor Material (LSAM)

Once the ability to produce quality hollow spheres of various ceramics was established, attention was shifted to determine the best method for incorporating them into a metal matrix. At first glance, such a process appears easy—pour them into the mold and then infiltrate with the desired matrix in either powder or molten form. However, this approach greatly oversimplifies the intricacy of the composite processing step. For example, early trials indicated that deliberate care and consideration must be taken to keep the hollow spheres properly spaced so that they are not fractured or crushed by impinging on each other during casting. Moreover, careful attention must be paid to processing conditions (e.g., temperature profiles) to minimize the extent of interfacial reactions between the metal matrix and reinforcing spheres. Although some reaction is desired to ensure a well-bonded interface, an overly extensive reaction can result in the formation of undesired compounds/intermetallics or weakening of the spheres due to the consumption of the sphere wall. Finally, when casting, the proper injection pressure is required to ensure the complete infiltration of the sphere preform without forcing liquid metal into the hollow spheres through pores in the walls. Although the majority of the efforts described in the following subsections involve aluminum alloys, DST has also demonstrated the ability to produce syntactic foams of other alloys (see Section 3.3).

3.1 Powder Metal Processing

As a first step, a powder-based processing approach for producing composite materials was used. This effort was achieved by layering aluminum powder and SiC spheres in an alumina crucible as illustrated in Fig. 16. The samples were fired at 680 °C under 650 Torr of argon for 30 min with a 10 °C per minute ramp. It was hoped that as the aluminum powder was heated, it would infiltrate the layer of the SiC spheres. As seen in Fig. 17, however, this did not occur. Instead, as the top aluminum powder layer melted, it formed a solid aluminum layer rather than infiltrating through the SiC spheres layer.
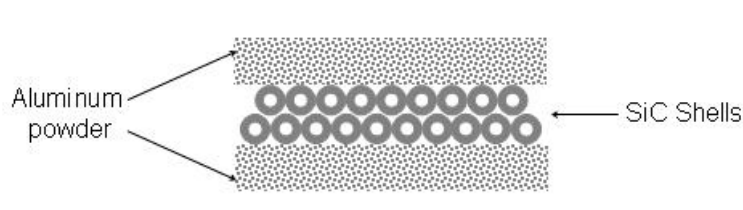
Fig. 16   Schematic detailing the starting arrangement for the powder-based approach to producing a syntactic foam

Fig. 17　Layers of aluminum powder and SiC spheres after being fired

In an effort to solve this issue, SiC spheres were mixed with aluminum powder and water to form a slurry, which was then dried into a paste that was subsequently transferred into alumina crucibles. These samples were then fired in a vacuum furnace under the same conditions as described earlier. However, the high self-affinity of aluminum created solid aluminum pockets that did not contain any spheres. Moreover, as shown in Fig. 18, it also appears that the packing content of the SiC spheres in the dried part was too high, further complicating the processing trial.

Fig. 18　Sample made from SiC spheres and aluminum powder slurry after being fired

Lastly, the SiC spheres were mixed with aluminum powder to form a dry mixture as illustrated in Fig. 19. The samples were subsequently fired in a vacuum furnace under the same conditions as described earlier. This method produced the best results of the powder-based methods. Indeed, as shown in Fig. 20 (left), a relatively flat piece of solid aluminum encapsulating SiC spheres was obtained. The sample was cut and SEM pictures of the cross section were taken (Fig. 20, right). It confirms the presence of hollow SiC spheres in a solid aluminum matrix. However, despite the limited success of this last approach, the powder-based methods typically resulted in poorly consolidated preforms, which often contained large

matrix regions that contained few, if any, spheres. Thus, attention shifted to liquid (e.g., casting) methods for producing the hollow sphere composites.
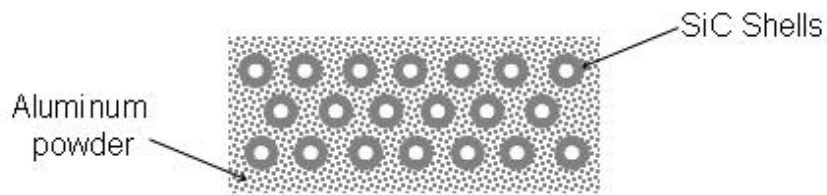
Fig. 19   Dry mixture of aluminum powder and SiC spheres
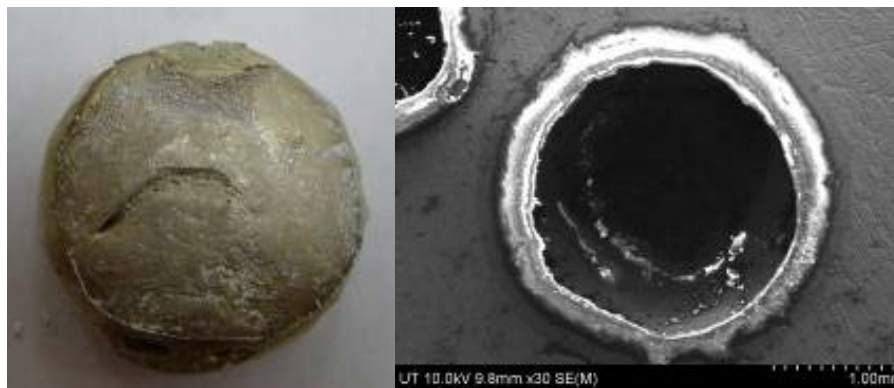
Fig. 20   Sample from dry mixture of SiC spheres and aluminum powder after being fired (left), SEM of a cross section of the sample (right)

3.2 Initial Casting Studies

A series of initial efforts at casting the molten metal into a hollow sphere "bed" revealed that the spheres were simply pushed along by the molten metal front as it entered the mold cavity. As a result, the concept of a filled preform was developed (Fig. 21). In addition to preventing sphere motion during infiltration, the preform also served to ensure proper spacing such that the spheres did not develop excessive point contact pressure loadings that resulted in fracture or collapse during the casting process.

Fig. 21   Densely packed preforms will need to support their own weight during the casting process

A key feature of these filled preforms was the use of inert fibers or particles (i.e., Saffil, carbon fibers, or SiC particulates) as well as a binder (aluminosilicate glass powder and starch) that was used to create a "solid" preform that separated the spheres during casting as well as the preheat process that occurs immediately prior to casting. As shown in Fig. 22, the preforms can be preheated over 600 °C outside the casting die and then rapidly transferred to the die immediately prior to the casting process.

Fig. 22   A preformed block of spheres being preheated prior to casting

Detailed experiments and analysis indicated that 500-grit SiC particulates performed the best at maintaining structural integrity during the preheating process. The Saffil fiber fills survived the burnout process but were brittle, difficult to handle at the preheat temperature, and inclined to crumble. The carbon fiber and binder only fills burned out completely and did not survive the preheat process. Figure 23

shows a set of plates produced with different preforms. Of the range of preforms used, the one composed of SiC particulates yielded the best syntactic foam plate.
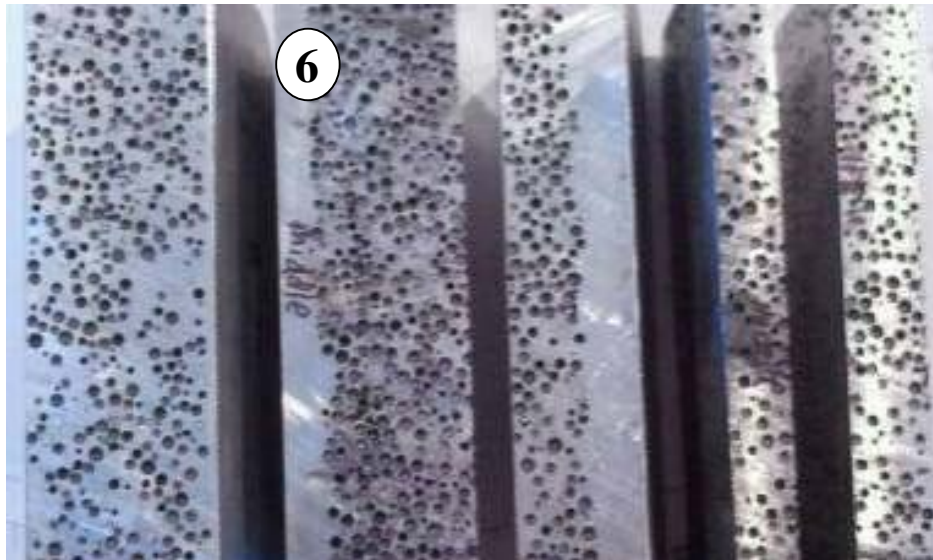
Fig. 23 **Samples obtained during the study to determine best "recipe" for use in constructing preformed sphere blocks. Sample 6 that used SiC particulates was found to have the most favorable results.**

3.2.1 Gravity Casting

In efforts prior to the start of this program DST had attempted to produce hollow sphere metal composites (10-mm diameter M350 spheres in aluminum) using gravity casting. However, these efforts met with minimal success (Fig. 24). Indeed, it was observed that the matrix fill was limited to the first inch of the casting (attempted panels were $6 \times 6 \times 1$ inches) resulting in cast specimens $6 \times 1 \times 1$ inches.
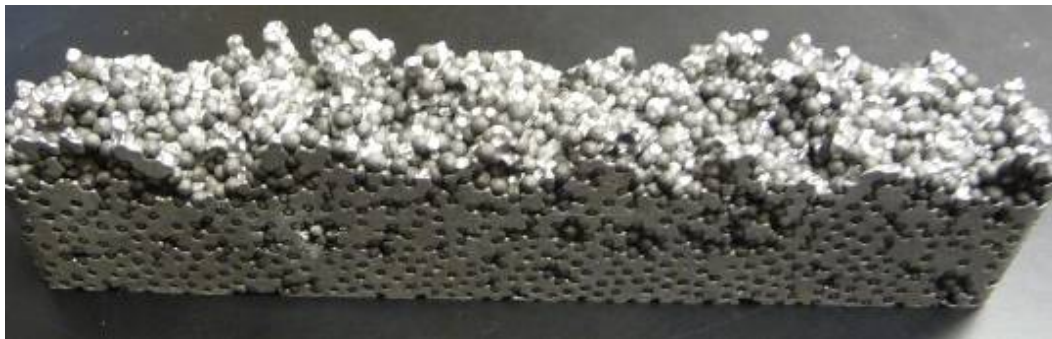
Fig. 24 **Early casting of M350 hollow spheres in an aluminum matrix**

Once the ability to produce high-quality ceramic spheres was established, an effort was made to use gravity casting to infiltrate 10-mm diameter SiC spheres with an

aluminum matrix (Fig. 25). These efforts met with a higher degree of success, which was attributed to the larger interstitial spaces present in this particular preform.

(a)

(b)

(c)
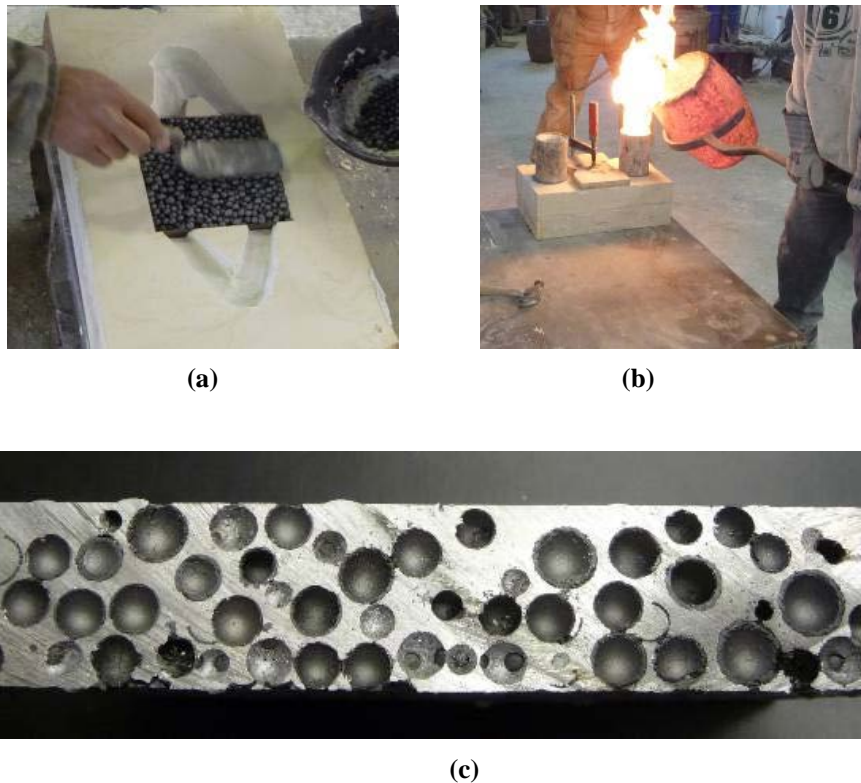
Fig. 25   Early casting of M350 hollow spheres in an aluminum alloy 319: a) 19-mm cavity fill, b) casting pour, and c) cross section of 10-mm SiC syntactic foam

3.2.2 Squeeze Cast SiC Spheres in AA5083 Matrix: Cast Pressure Study

Several different casting pressures were undertaken during the infiltration of the hollow SiC sphere preforms. Pressures investigated were approximately 35–50 MPa. These plates were cast with hollow SiC spheres at a 46% volume fill, with SiC particulate fill and 4% binder holding the preform together. The best results, as indicated by the lowest fraction of filled or broken spheres combined with complete sphere wetting and void free matrix, were achieved with approximately 38 MPa pressure during infiltration of the AA5083 matrix material. Plates from these trials can be seen in Figs. 26 and 27.

Fig. 26   SiC hollow-sphere-filled AA5083 syntactic metal matrix composite 9- × 13-inch plates were cast at various pressures to establish optimum casting conditions

| (a) | (b) |
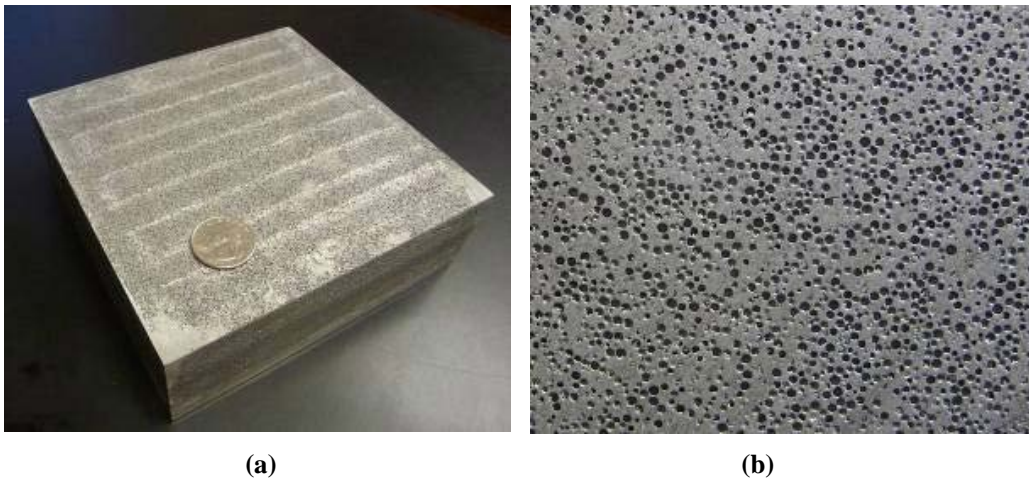
Fig. 27   a) A1/SiC hollow sphere syntactic block of size 6 × 6 × 2 inches, and b) close-up of syntactic surface

Recognizing the need to reduce or eliminate matrix-filled hollow spheres, DST developed a method to screen the spheres for holes. Spheres from the same fabrication lot as those used in the casting shown in Fig. 28 were prescreened at DST and sent to CPS Technologies for casting trial. The result was a composite material (Fig. 29) having a significantly lower density of 1.62 g/cm^3, which is 60% of the base (aluminum) material.
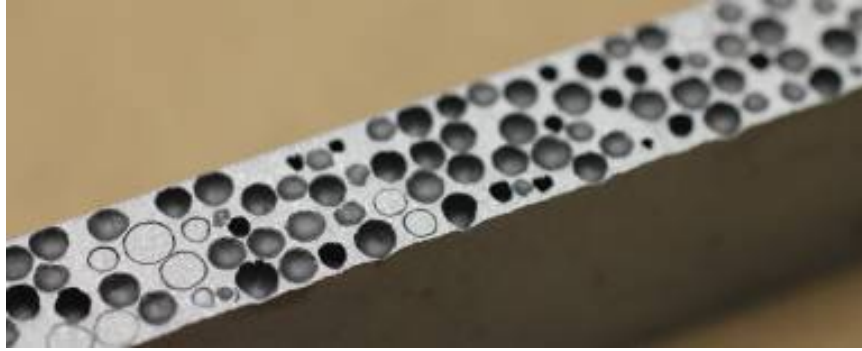
Fig. 28   Initial pressure-casting trial of Al/SiC hollow sphere syntactic foam (in conjunction with CPS Technologies)
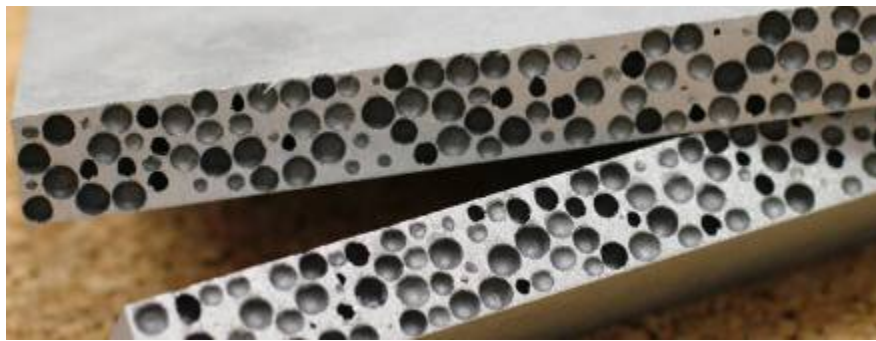
Fig. 29   Second pressure-casting trial (in conjunction with CPS technologies)

3.3 Other Alloys

As seen in the previous sections, the majority of the casting research and development performed by DST has focused on aluminum alloys. However, as seen by the following examples, DST has successfully translated the knowledge gained from these efforts into other alloy systems of interest.

One alloy system that was of great interest to DST was the magnesium-based alloys. As these alloys already have the lowest density of the structural metals (aluminum, titanium, steel, etc.), it was thought that a magnesium syntactic foam could offer extremely good specific properties accompanied by appreciable weight savings. As shown in Fig. 30, DST was able to produce an Al_2O_3/AZ91 syntactic foam with a good sphere distribution and surface quality. The combination of alumina spheres and magnesium alloy resulted in this syntactic foam having a density of approximately 1.15 g/cm^3. In an effort to make a foam with an even lower density, SiC spheres were encapsulated in an AZ91 matrix. Given the approximate sphere content of 48%, the density of the syntactic foam is approximately 0.95 g/cm^3, which is less than a density of 1.0 g/cm^3 needed for self-buoyancy. As a result, this syntactic foam will actually float in water, as shown in

Fig. 31. Despite DST's proven ability to produce high-quality magnesium syntactic foams, this area of research has not been vigorously pursued due to the negative mindset of many potential customers toward magnesium alloys.
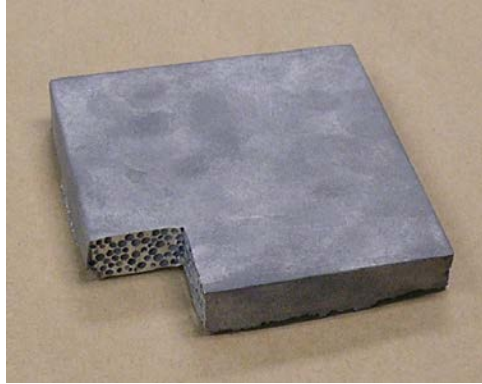
Fig. 30   Hollow Al$_2$O$_3$ shells in Mg-alloy (AZ91) matrix
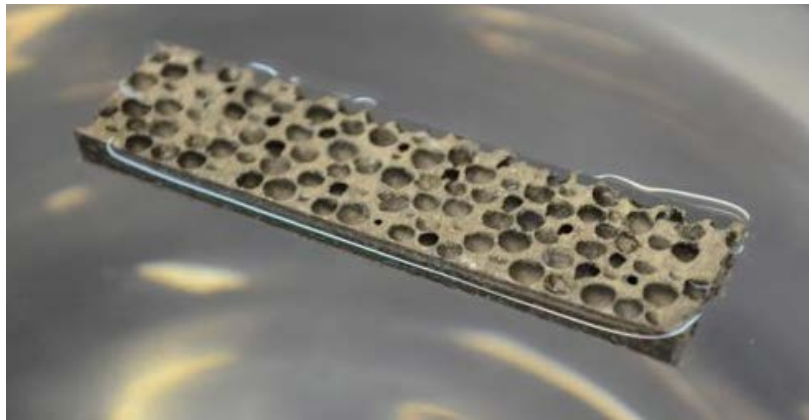
Fig. 31   SiC/AZ91 syntactic foam that floats

4.   Testing and Characterization of LSAMs

During the course of this study, a large number of syntactic foams were processed and evaluated for a variety of physical and mechanical properties. This section will provide brief descriptions of these efforts to provide further insight into the versatility of these materials and their potential applications.

4.1 Finite Element Modeling of the Quasi-static Deformation

To develop an understanding for the response of the LSAMs, a series of finite element models was developed and subsequently used for virtual experiments. For these studies, a magnesium alloy (AZ91D) containing M350 hollow spheres was constructed. In the model, the hollow spheres are assumed to be perfectly spherical

with a diameter of approximately 2.5 mm and wall thickness of 0.06 mm. The size of the 2-D sample simulated is set at 10×10 mm^2, with a mesh density of 20. The details of the parameters involved in the simulation are listed in Table 1.

Table 1   Parameters used for the modeling of M350 maraging steel spheres embedded in an AZ91D alloy matrix

Parameter	AZ91D	M350
Yield tensile strength (MPa)	140	827
Young's modulus (GPa)	45	211
Poisson's ratio	0.35	0.3
Density (g/cm^3)	1.84	8.08
Tangent modulus (MPa)	2241.4	1758.4
Elongation at break	0.035	0.18

A program was written to create the 2-D geometry for the AZ91 alloy/maraging steel hollow sphere composite material. Figure 32 shows an example of the geometry that is being investigated. The spheres are placed in the sample space following Gaussian normal distribution, and the total volume accrues as more spheres are embedded until the desired total volume fraction of 40% is reached. The von Mises stress patterns at varying strain levels are shown in Fig. 33 along with corresponding logarithmic strain distributions.
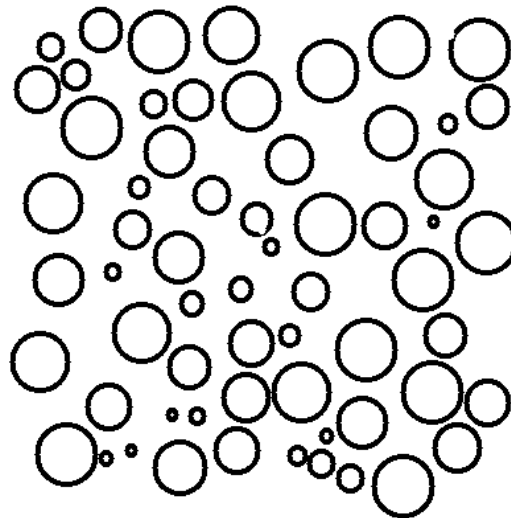
Fig. 32   The 2-D geometry of AZ91D/maraging steel lightweight syntactic foam (10×10 mm^2)
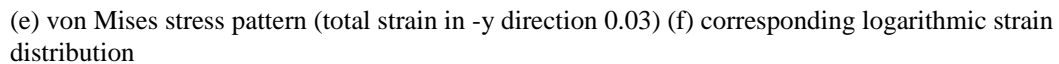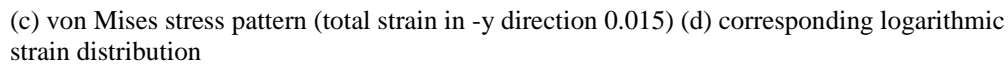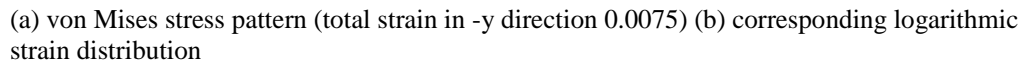
(a) von Mises stress pattern (total strain in -y direction 0.0075) (b) corresponding logarithmic strain distribution

(c) von Mises stress pattern (total strain in -y direction 0.015) (d) corresponding logarithmic strain distribution

(e) von Mises stress pattern (total strain in -y direction 0.03) (f) corresponding logarithmic strain distribution

Fig. 33 The von Mises stress patterns and total logarithmic strain distributions of 10- × 10-mm^2 AZ91D/M 350 hollow sphere composite material under –y direction strain of a) and b) 0.0075; c) and d) 0.015; e) and f) 0.03; g) and h) 0.045; and i) and j) 0.06

23
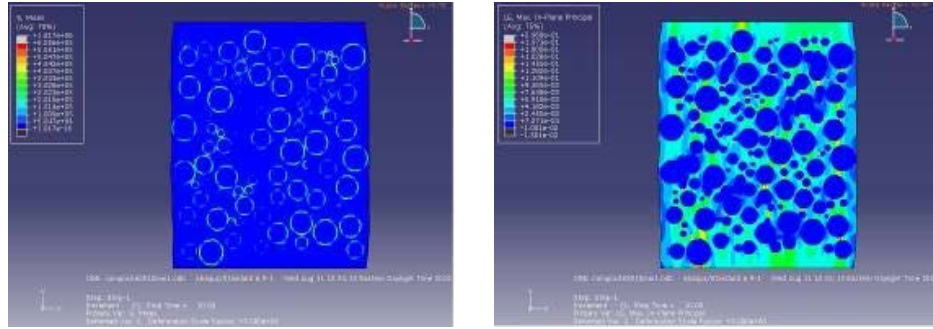
(g) von Mises stress pattern (total strain in -y direction 0.045) (h) corresponding logarithmic strain distribution
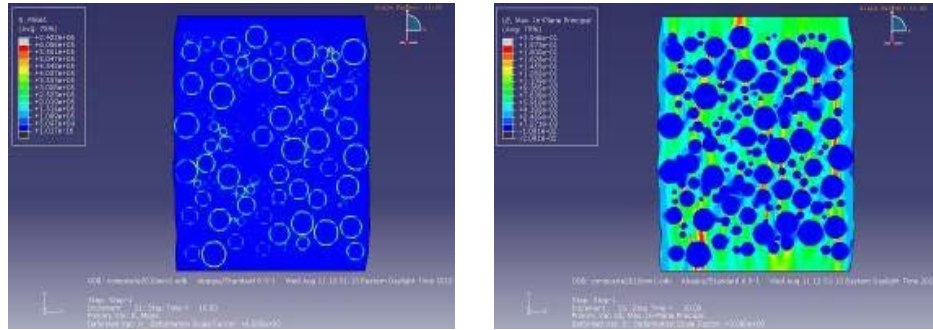
(i) von Mises stress pattern (total strain in -y direction 0.06) (j) corresponding logarithmic strain distribution

Fig. 33   The von Mises stress patterns and total logarithmic strain distributions of 10-× 10-mm² AZ91D/M 350 hollow sphere composite material under –y direction strain of a) and b) 0.0075; c) and d) 0.015; e) and f) 0.03; g) and h) 0.045; and i) and j) 0.06 (continued)

The deformation of the sample has been augmented by 8 times for the viewers' convenience. The actual maximum strain in –y direction is only 0.06. As clearly seen in the stress pattern, the circumferences of the embedded spheres are the places where the stress concentrates, whereas the alloy matrix sustains most of the strain. The tensile stress mostly concentrates around the interface between the embedded spheres and the alloy matrix while the matrix exhibits the majority of the deformation.

For each sphere, the sphere's mass (m) and average diameter (d_{avg}) are measured and then used to calculate the sphere density (ρ_s), as well as the relative density (f_v) and wall thickness (t_w) (Eqs. 8–10). In the modeling effort, the influence of various sphere wall thicknesses was determined.

$$\rho_s = \frac{m}{\frac{4}{3}\pi \left(\dfrac{d_{avg}}{2}\right)^3} \quad . \tag{8}$$

$$f_v = \frac{\rho_s}{\rho_0} \quad . \tag{9}$$

$$t = \frac{\left(\dfrac{d_{avg}}{2}\right) f_v}{3} \quad . \tag{10}$$

Substituting in the appropriate values for wall thickness (0.12 mm) and average sphere diameter (2.5 mm) yields a relative density of 0.288. To examine the effects of the relative density, the diameter and the total sphere volume fraction was held constant while the wall thickness was varied from 0.12 mm to 0.18 mm and 0.24 mm, while the relative density varied from 0.288 to 0.432 and 0.576. The accompanying geometries of the composite materials are shown in Fig. 34, with the resulting final von Mises stress patterns and strain localization distributions shown in Fig. 35.
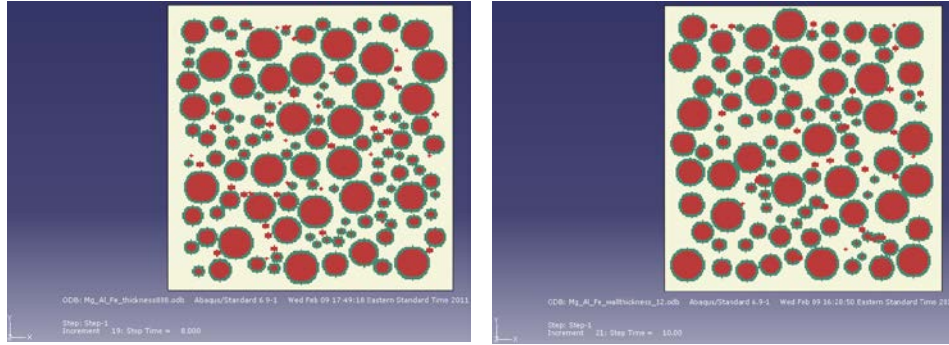
(a) sphere wall thickness 0.18 mm　　　　(b) sphere wall thickness 0.24 mm

Fig. 34　The 2-D geometry of AZ91D/maraging steel hollow sphere (20×20 mm^2) with the sphere wall thickness at a) 0.18 mm and b) 0.24 mm

(a) von Mises stress pattern (wall thickness 0.18 mm)   (b) logarithmic strain distribution

 (c) von Mises stress pattern (wall thickness 0.24 mm) (d) logarithmic strain distribution
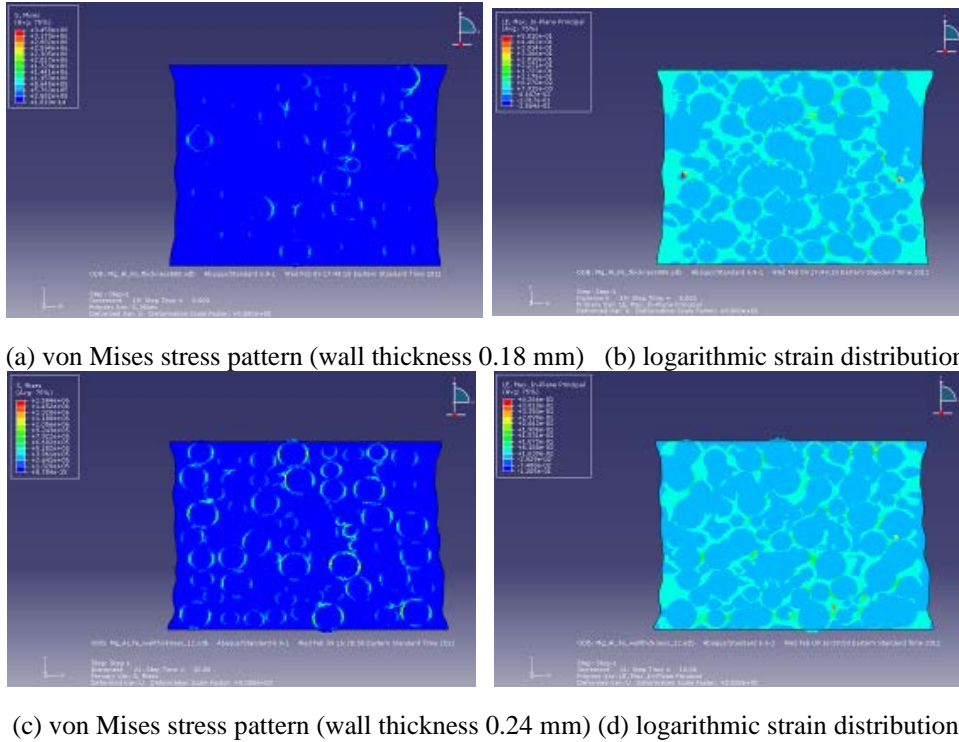
**Fig. 35   The von Mises stress patterns and total logarithmic strain distributions of 20-×
20-mm² AZ91D/M 350 LSAM with sphere wall thickness at a) and b) 0.18 mm and c) and d)
0.24 mm**

The calculated stress-strain curves with increasing sphere wall thickness are
displayed in Fig. 36. Not surprisingly, the composite material with thicker sphere
walls witnesses an uptick in both the Young's modulus and the yield strength. The
106% and 118% increase observed in the modulus and yield strength when the wall
thickness increases from 0.12 mm to 0.18 mm and 0.24 mm can be explained by
the fact that the thicker sphere wall provides more resistance when the spheres start
to impinge upon each other due to the external force. Although the results indicate
that a sphere with a thicker wall performs better, the final choice of sphere
dimensions must be balanced by considering the desired final density (or weight)
of the syntactic metal foam.
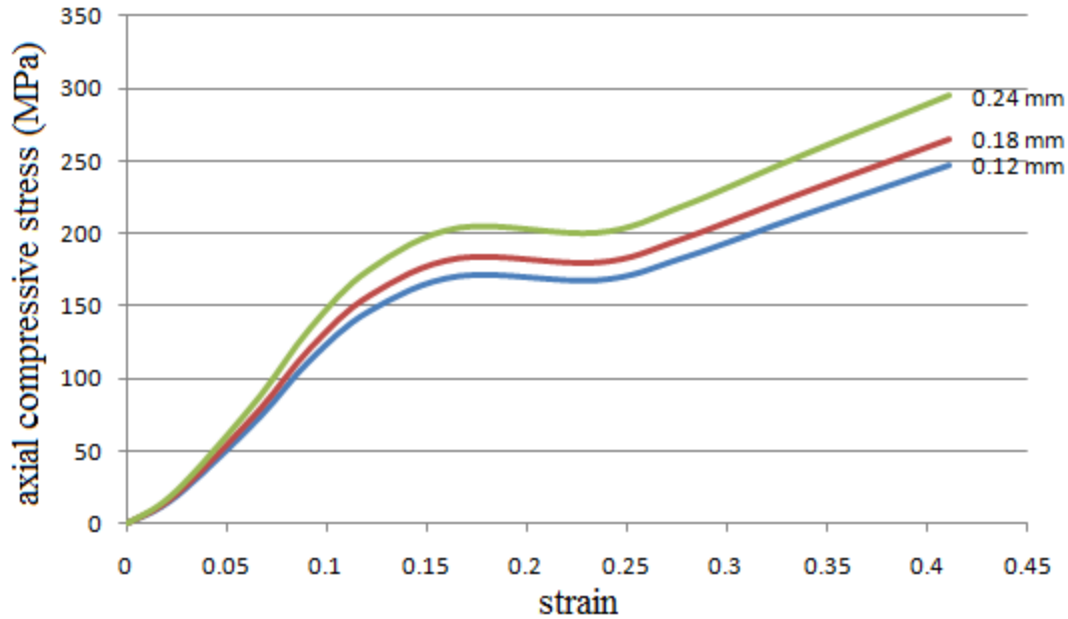
Fig. 36 **Compressive stress-strain curves of the AZ91D/M350 sphere syntactic foam with different sphere wall thicknesses**

4.2 Compressive Response at Quasi-static and High Strain Rates (Luong et al. 2013)

Aluminum/SiC is one of the most widely studied aluminum matrix composite (AMC) systems. Aluminum alloys and AMCs have been used to replace steel in automotive body panels, engine components, and brake rotors to reduce structural weight, which has resulted in increased interest in these materials. In this work performed with Professor N Gupta at New York University, SiC hollow-sphere-filled A356 matrix syntactic foams are developed and characterized for quasi-static and dynamic compressive properties.

4.2.1 Materials and Methods

SiC hollow spheres with nominal diameter and wall thickness of 1 mm and 70 µm, respectively, were encapsulated in an A356 matrix using pressure infiltration. The approximate volume percent of the SiC spheres was 60%. The specimens did not have any measurable porosity in the matrix, as confirmed by extensive microscopy. The density of the synthesized syntactic foams was measured to be 1.819 g/cm^3.

The quasi-static compression testing was conducted using an Instron 4469 test system equipped with a 50-kN load cell. Cylindrical specimens with nominal diameter and length of 10 and 5 mm, respectively, were used for compression testing. To minimize the effect of friction, 111 Valve Lubricant and Sealant (Dow Corning, Midland, Michigan) was used at contact surfaces between the specimen

27

and compression platens. The high-strain-rate compression tests were conducted using a Split-Hopkinson pressure bar (SHPB) setup. Cylindrical specimens of nominal 10-mm diameter and 5-mm thickness were used for testing. Optical and electron microscopy were used to examine the specimens in the as-processed condition as well as after testing.

4.2.2 Results

4.2.2.1 Microstructure

The microstructure of as-fabricated A356/SiC syntactic foam is shown in Fig. 37 at 2 different magnifications. These optical micrographs show high survival rate of the SiC spheres in the matrix after the pressure infiltration process. All the SiC spheres visible in these figures are intact and are not infiltrated by the matrix. Figure 37b shows some closely spaced particles. A thin layer of matrix alloy can be clearly observed in the interparticle region of closely spaced hollow spheres, which indicates good wetting at the matrix-sphere interface.

(a)	(b)
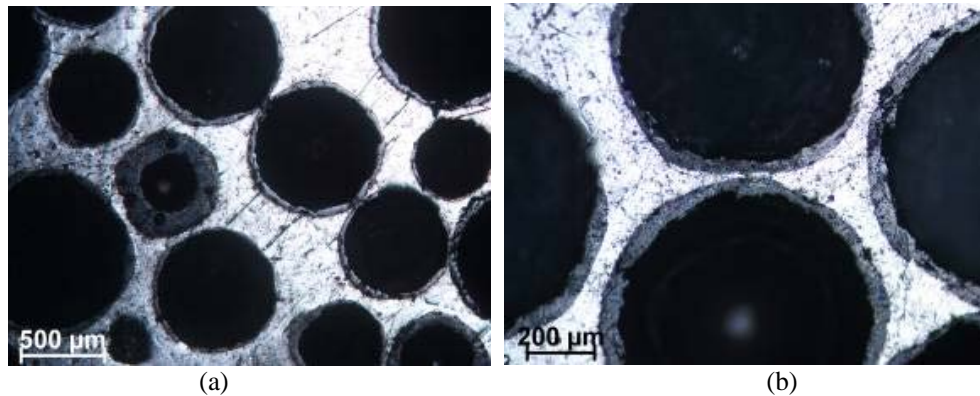
Fig. 37   Optical micrographs of A356/SiC syntactic foam showing particle distribution in the composite. The particles are wetted well with the alloy, as even the closely spaced particles have a layer of matrix between them.

4.2.2.2 Quasi-static Compression

Quasi-static compressive stress-strain curves of A356/SiC syntactic foams are presented in Fig. 38. The beneficial characteristic observed in the compressive behavior of syntactic foams is large deformation strain, which is helpful in obtaining a high level of energy absorption in these materials. The quasi-static compressive properties measured on 5 specimens of syntactic foams are presented in Table 2. In this table, the compressive strength is defined as the peak stress at the end of the initial linear elastic region, and plateau stress is defined as the stress level after the initial drop. The stress plateau is not very stable in these specimens and an increasing trend with small slope is seen. The reported value is calculated as the

average from the start of the plateau to the densification strain. The densification strain is defined as the strain in the plastic region where stress exceeds the compressive strength value. The average values of compressive strength, plateau stress, and densification strain are 163, 110, and 0.46 MPa, respectively.
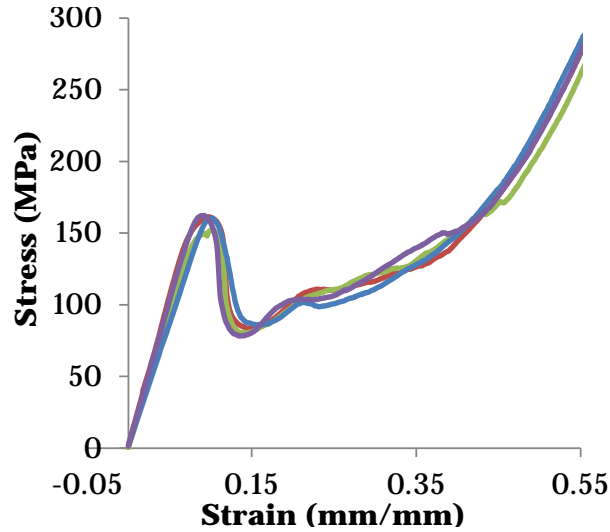
Fig. 38   Quasi-static compressive stress-strain graphs of A356/SiC syntactic foam

Table 2   Quasi-static compressive properties of A356/SiC syntactic foams

Specimen	Modulus (GPa)	Compressive strength (MPa)	Plateau stress (MPa)	Densification strain (mm/mm)
1	2.08	161	107	0.46
2	1.85	152	111	0.48
3	1.71	161	102	0.42
4	2.02	162	105	0.48
5	2.10	181	126	0.45
Average	1.95	163	110	0.46
St. Dev.	0.17	11	9	0.03

4.2.2.3   Dynamic Compression

The majority of the stress-strain graph in Fig. 39 is obtained under an average high strain rate of 970 s^{-1}. The general trend of dynamic stress-strain graphs is similar to quasi-static compression graphs, where a linear elastic region is followed by drop in stress after the peak strength is reached. The strain in dynamic testing is limited to the pulse width observed in this figure, which is dependent on the striker bar length. Therefore, densification strain is not obtained in dynamic stress-strain graphs. The calculated dynamic mechanical properties are presented in Table 2. The modulus data should be treated with caution in SHPB testing. Figure 39 shows

that the strain rate rises sharply in the initial part of the stress-strain curve. This part is avoided during modulus calculation and only the region that corresponds to constant strain rate is used for calculation. If the constant strain rate region is not obtained until the peak stress is reached, the modulus cannot be calculated in this kind of testing. A comparison of quasi-static and dynamic properties in Tables 2 and 3, respectively, shows that the compressive properties of A356/SiC$_{HS}$ syntactic foams are not strain rate sensitive. The peak strength value obtained from the dynamic test is 123.5 ± 3.8 MPa. As the strain rate sensitivity is dependent on strain rate, the present conclusions are limited to the strain rate range used in this work.
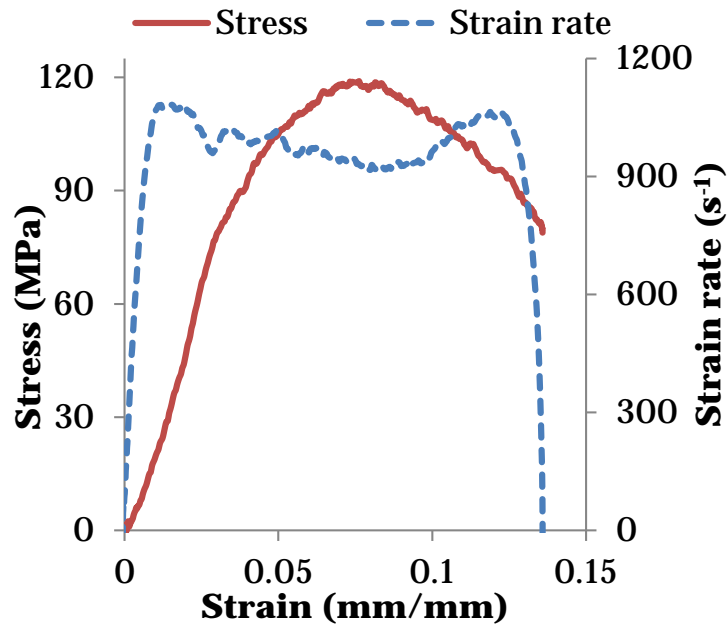
Fig. 39   Representative strain rate-strain and stress-strain graphs obtained from high-strain-rate tests of an A356/SiC syntactic foam tested at a strain rate of 970 s^{-1}

Table 3   High-strain-rate properties of A356/SiC syntactic foams measured from SHPB testing

Specimen	Strain rate (s^{-1})	Compressive strength (MPa)	Modulus (GPa)
1	940	124.5	4.7
2	970	119.0	3.0
3	1160	125.5	5.2
4	1165	123.0	3.6
5	1220	120.7	5.7
6	1310	119.3	3.0
7	1425	130.1	3.5
8	1520	125.7	5.8

4.2.2.4   Failure Analysis

The microstructure of as-fabricated specimens obtained from the SEM is presented in Fig. 40. Uniformity in the distribution of the SiC spheres can be seen in this figure. A closer observation shows that cracks exist in some of the SiC spheres (Fig. 41), which may have occurred during composite fabrication.

(a)   (b)
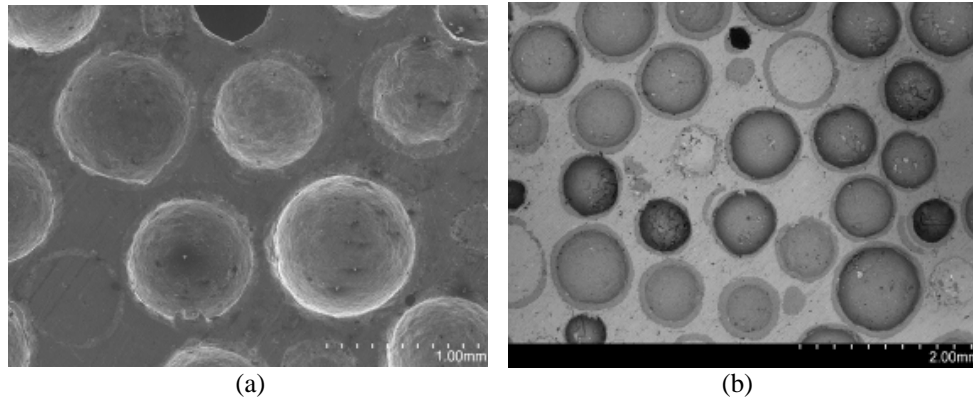
Fig. 40   SEMs of an as-fabricated A356/SiC syntactic foam obtained using a) secondary electron and b) backscattered detector
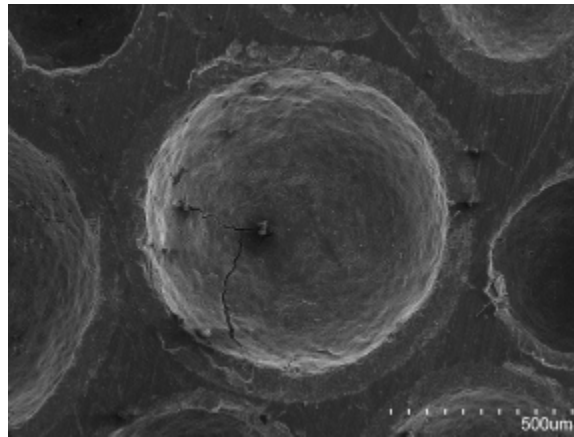
Fig. 41   Cracks noticed in one of the hollow spheres

The failure pattern in syntactic foams was observed using a high-resolution digital camera equipped with a telephoto lens. Figure 42 illustrates a quasi-static compressive stress-strain diagram of A356/SiC syntactic foams. Six locations corresponding to various optical photographic observations captured in Fig. 43 are identified in this figure. The as-processed specimen is shown in Fig. 43a. During the elastic deformation, no SiC sphere failure is observed, as seen in Fig. 43b. As the stress peak is reached, failure of the SiC spheres begins, as captured in the hollow sphere marked by a circle in Fig. 43c. Some of the spheres with pre-existing cracks, seen in the as-fabricated composite in Fig. 7 may initiate failure. The initial

SiC sphere failure can be due to 1) the defects such as cracks present in the hollow sphere walls, 2) relatively thin-walled hollow spheres that may have lower strength than other hollow spheres, or 3) localized stress concentrations resulting from factors such as a group of closely spaced spheres. Cracks in the loading direction of the SiC spheres are observed in Fig. 43c. This pattern is similar to the failure of several other SiC particles observed during compression. Figure 43d shows that the cracks can extend to the matrix material in the same direction, which is likely due to the strong interfacial bonding of the SiC spheres with the matrix. Figures 43e and 43f correspond to plateau regions where progressive densification takes place. These figures show various locations of SiC sphere collapse, localized large matrix deformation, and densification of porosity due to compaction of material. Shear cracks in the matrix are also observed during this stage, which lead to SiC sphere fragmentation. The hollow sphere crushing and densification in the shear band progressively increases and leads to complete densification of the specimen.
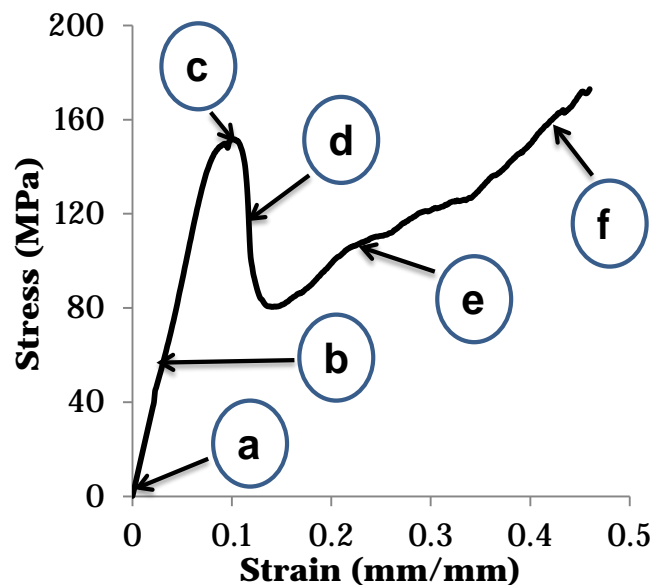
Fig. 42   Locations on stress-strain diagram for observations presented in Fig. 43
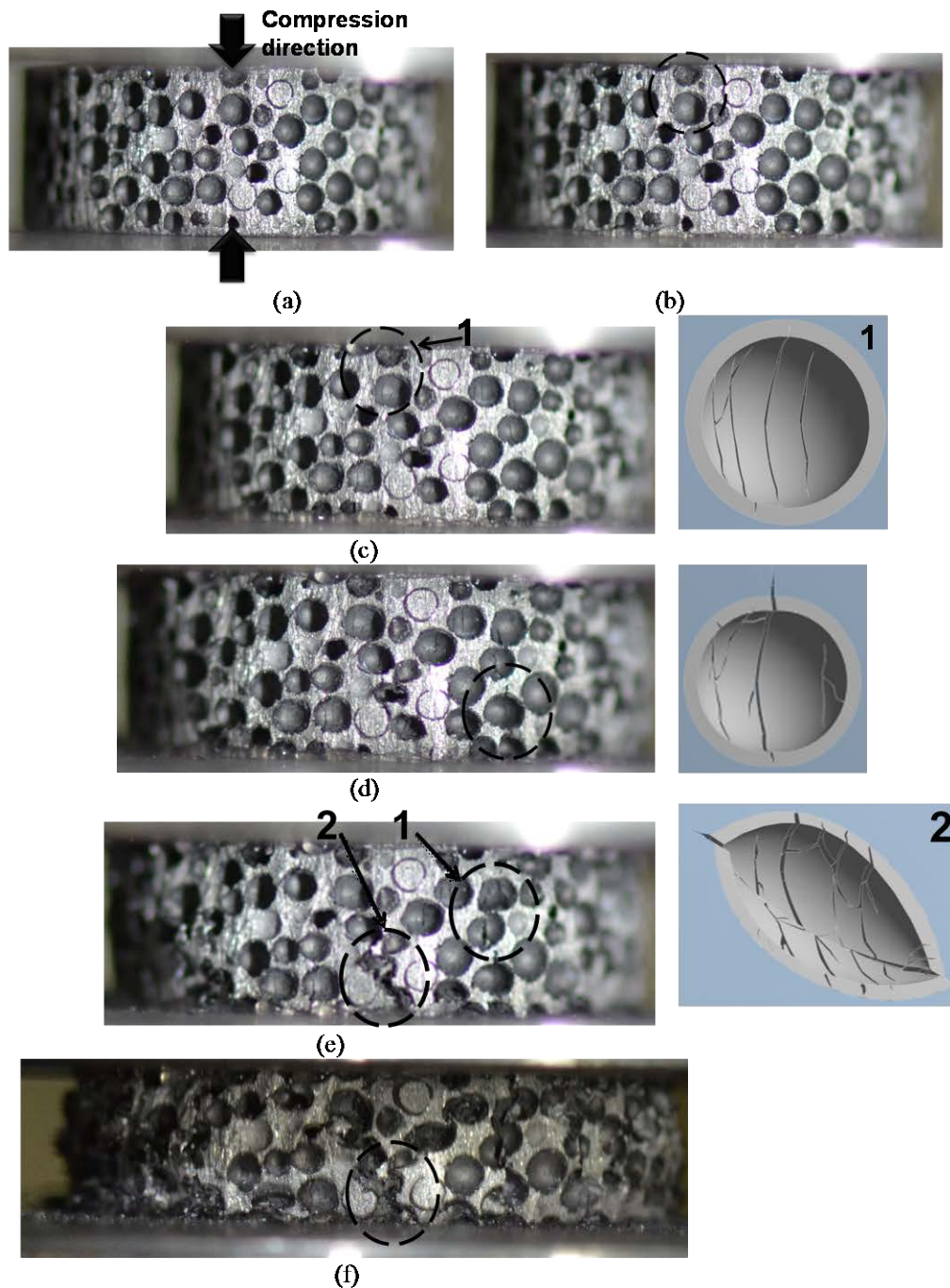
Fig. 43 Observations of various stages of material failure in A356/SiC$_{HS}$ syntactic foams: a–f) correspond to successive stages of quasi-static compressive failure as represented in Fig. 42. Failure mechanisms marked with 1 and 2 are displayed in sketches included in c) and e), respectively.

Specimens that failed under quasi-static loading condition are further analyzed using the SEM. The micrographs are shown in Fig. 44. The specimens are sectioned in the loading direction using an Isomat diamond blade saw and the micrographs are taken on the as-cut surface. SiC spheres are completely crushed in the specimens at complete densification, as observed in these micrographs. Backscattered electron images in Figs. 44b and 44d clearly show the hollow sphere and the matrix phases. Complete densification of porosity is observed in these figures due to extensive plastic deformation of the matrix.

| (a) | (b) |
| (c) | (d) |
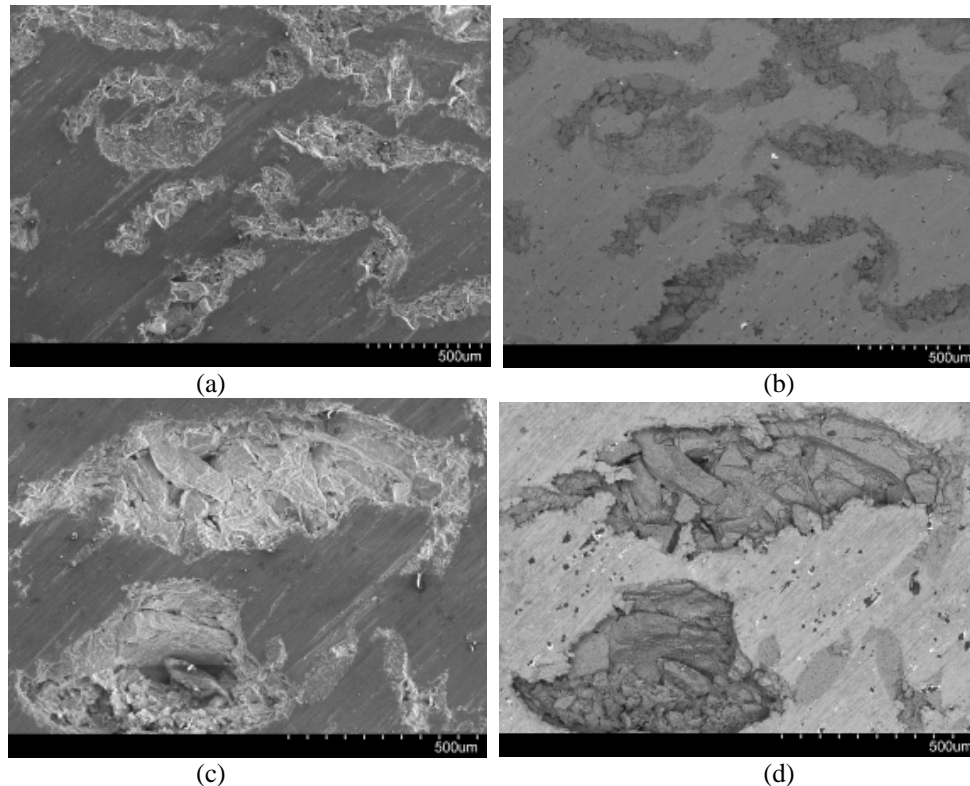
Fig. 44   Specimens failed and densified under quasi-static compression: a) and c) secondary electron, and b) and d) backscattered electron SEM images. Particle crushing can be observed without interfacial separation.

A356/SiC foams subjected to high-strain-rate compression are also analyzed for failure features. A lower magnification image of a failed specimen is shown in Fig. 45a. A shear band can be observed in this image, marked by a rectangle. SiC spheres along this band have crushed and their cavities are consumed by the compressing material as observed in Fig. 45b. Large-scale matrix deformation in this region has resulted in compaction of debris, without the presence of matrix cracks in the vicinity. Spheres shown in Fig. 45a, which are not directly on the shear band, have developed cracks and fractured under compression as per the mechanism demonstrated in Fig. 45c. These hollow spheres did not show signs of

shearing at this stage. The formation of the first shear band will depend on the presence of weak spheres along a plane, but eventually additional shear bands generate and all the hollow spheres fracture and densify as the compression reaches densification strain.

(a)

(b)

(c)
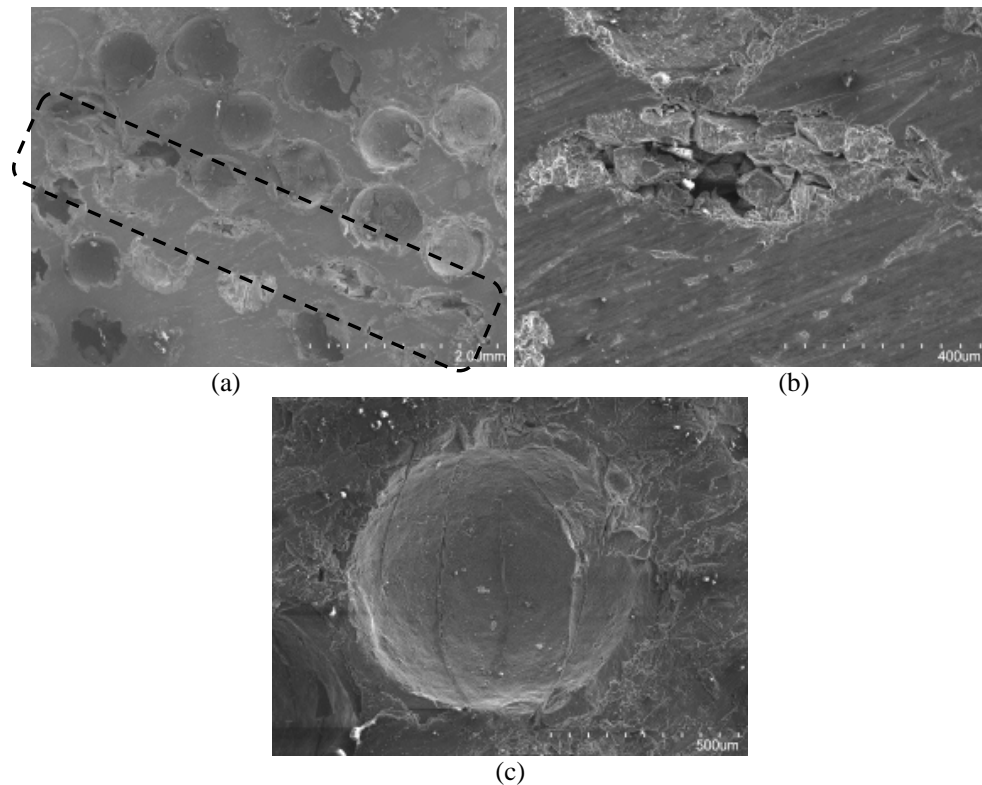
Fig. 45   SEM of A356/SiC syntactic foam tested at 1,220 s^{-1} strain rate. a) A shear band with hollow sphere failure is observed, b) close observation of a particle failed along shear band, and c) failure of a particle away from the shear band; cracks in the loading direction initiate and cause failure of the particle.

4.2.3 Conclusions

Aluminum alloy A356/SiC hollow sphere reinforced syntactic foams were studied in both quasi-static and dynamic compression. Clear evidence of hollow sphere failure at the peak stress is obtained. The failure initiates by the fracture of weak particles, with some of the cracks propagating through the matrix as well. Shear band formation in the matrix and shearing of SiC spheres ultimately results in failure. In addition, it was observed that the debris of hollow spheres is compacted in their own cavity and densification is obtained. The compressive strength and plateau strength are measured as 163 and 110 MPa, respectively, for composites

having 60 vol% SiC hollow spheres. Finally, strain rate sensitivity was not observed in any samples tested up to a strain rate of 1,520 s^{-1}.

4.3 Thermal Properties of A356/SiC Syntactic Foam (Cox et al. 2014)

4.3.1 Materials and Methods

A356 alloy was used to synthesize syntactic foams by using a pressureless infiltration method in a bed of hollow SiC particles. Two sample types were studied, referred to as S1 and S2, with measured densities of 1.71 ± 0.06 and 1.84 ± 0.03 cm^3, respectively. The mean particle diameter is 1 mm for both spheres with a wall thickness of 67.8 ± 13.6 and 79.3 ± 20.5 μm, respectively, for sample types S1 and S2. The density is calculated by measuring the dimensions and weight of compression test specimens. The volume fraction of SiC hollow spheres for both syntactic foams was approximately 60%.

A Q800 (TA Instruments, New Castle, Delaware) dynamic mechanical analyzer (DMA) was used to test the specimens at a constant frequency of 1 Hz in the temperature range of 35–510 °C under 3-point bend configuration. A static force of 1 N was applied at the midpoint of the specimen and the span length was fixed at 50 mm. The nominal dimensions of the syntactic foam specimens were 10.5 mm in width, and 3.5 mm in thickness. The pins were roller supported to provide uniform loading on the material and to inhibit friction effects.

The coefficient of thermal expansion (CTE) was determined using a Q400 thermo-mechanical analyzer from TA Instruments (New Castle, Delaware). The specimens were tested from an initial temperature of 35–405 °C at the ramp rate of 10°C/min. A preload force of 0.05 N was applied. The specimens had a nominal height and diameter of 10.5 and 10.0 mm, respectively. The glass probe that measures the dimensional change and applies the preload on the specimen was placed directly at the center at the top surface of the specimens. The CTE (α) was determined by

$$\alpha = \frac{1}{l}\frac{dl}{dt},\tag{11}$$

where l is the initial specimen height and t is time and dl/dt denotes the slope of the change in specimen height over the change in temperature.

4.3.2 Results

The storage and loss moduli for the syntactic foam as a function of temperature are shown in Fig. 46. The results of the A356 alloy obtained from the literature are shown for comparison. Both syntactic foams show similar behavior for storage and loss moduli, with the storage modulus decreasing with temperature while the loss modulus shows a slight increase with temperature. As seen in Fig. 47, the storage modulus-temperature profile is nearly linear for the foams, while the monolithic alloy shows a bilinear curve, with a steep decrease in storage modulus above 375 °C. In contrast, the loss modulus for both the foams and the alloy increases with temperature. Unlike the storage modulus, the loss modulus of the alloy is comparable to that of syntactic foams at low temperature. However, at temperatures above 250 °C, the loss modulus of the alloy starts to increase rapidly and shows a peak around 460 °C. In contrast, the syntactic foams display a more stable thermal behavior, with no evidence of peak within the test temperature range. The ratio of loss to storage modulus is defined as the damping parameter Tan δ. The damping parameter of syntactic foams is higher than that of the alloy at temperatures below about 425 °C as observed in Fig. 47. Above this temperature, the damping parameters of the foams and the alloy become nearly the same. The porosity in the walls of hollow spheres is expected to help in obtaining higher damping in the syntactic foams.
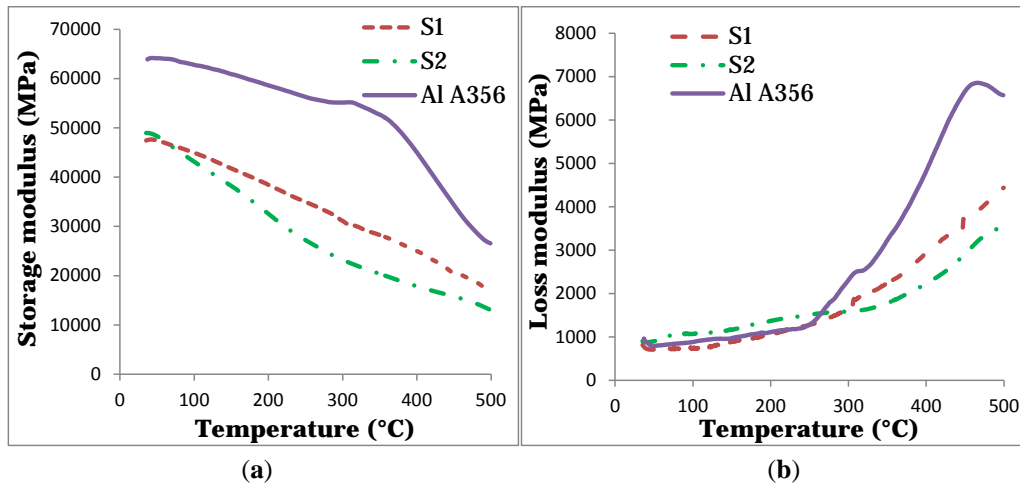
Fig. 46   a) Storage modulus and b) loss modulus with respect to temperature for the 2 syntactic foams and the matrix alloy
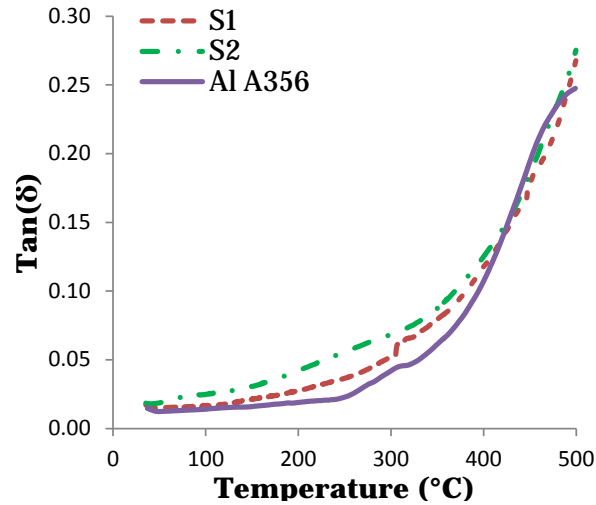
Fig. 47 Tan δ with respect to temperature for the 2 different types of syntactic foams and for the matrix alloy

The values of storage modulus, loss modulus, and Tan δ are extracted from the graphs at 3 different temperatures of 50, 200, and 400 °C and are presented in Table 4. These temperatures are arbitrarily selected to cover different trends and observe the difference in values. The properties can be extracted at any other temperature of interest based on the applications of these materials. There are some important trends to note in this table. The lack of viscoelasticity in the aluminum alloy results in a storage modulus that is nearly the same as the elastic modulus. The loss modulus is almost negligible compared to the storage modulus. For example, the loss modulus for the alloy is only 1.4% that of the storage modulus at 50 °C. Tan δ is also negligible at 50 °C. As the temperature is increased, the stiffness of the material decreases, which is reflected in a reduced storage modulus. Correspondingly, the loss modulus increases. At 400 °C the loss modulus for the alloy is 12% that of the storage modulus and Tan δ increased to 8.6 times relative to the value observed at 50 °C. Similar level of changes are observed in the properties of syntactic foams. The difference in the stiffness of the hollow spheres and matrix is expected to help in damping behavior at high temperatures by causing deformation along the sphere-matrix interface.

Table 4   Thermal properties of A356/SiC syntactic foams

Sample	Storage modulus GPa (50, 200, 400) °C	Loss modulus GPa (50, 200, 400) °C	Tan δ (50, 200, 400) °C
S1	47.45, 37.69, 25.79	0.70, 1.04, 3.22	0.015, 0.028, 0.125
S2	48.88, 32.57, 17.84	0.90, 1.39, 2.40	0.018, 0.043, 0.134
A356	69.22, 63.42, 48.07	0.98, 1.19, 5.79	0.014, 0.019, 0.120

Figure 48 shows micrographs of a specimen after DMA testing. Cracks in the SiC hollow sphere can be observed in this figure after the testing. Oxide layer formation on the aluminum alloy matrix also takes place due to high temperature during the testing. The images included in Fig. 48 do not show interfacial failure between particle and matrix, likely due to the surface porosity on the SiC hollow sphere leading to mechanical bonding with the matrix.

(a)   (b)
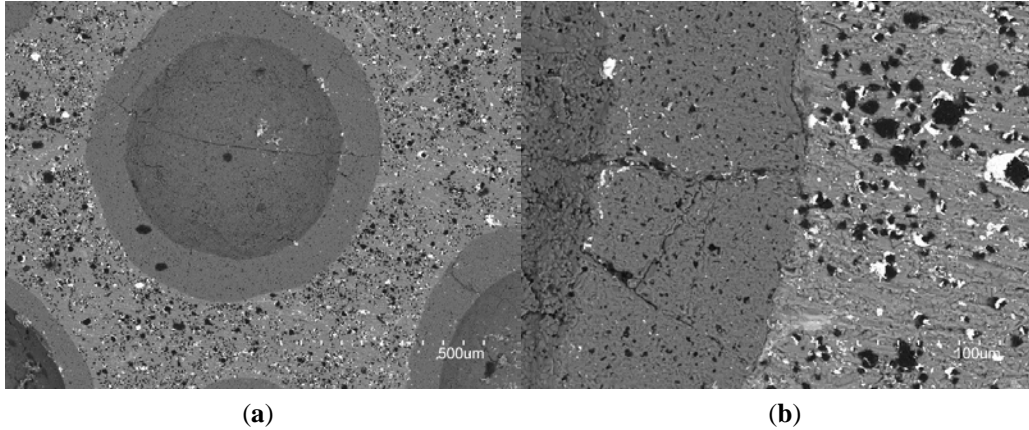
Fig. 48   a) Micrograph of S2 type A356/SiC syntactic foam after DMA test. b) The images show cracks in the SiC hollow particle wall and oxide formation on the surface of matrix surrounding the particle.

A representative thermal strain curve with respect to temperature is shown in Fig. 49 for a randomly selected S1 syntactic foam specimen. The curve shows 2 different linear regions used to calculate the CTE values, which are summarized in Table 5 for temperature ranges 100–200 °C and 300–400 °C. The percent change from the lower temperature range to the higher temperature range is 40.1 % and 38.7 % for the S1 and S2 samples, respectively. The S1 and S2 foams had average CTE values of 14.60 ± 0.91 and 15.74 ± 0.70 ($\times 10^{-6}$ °C^{-1}), respectively. A comparison of the CTE value of 23.4×10^{-6} °C^{-1} for the A356 alloy with the values of the 2 syntactic foams clear shows that the addiction of SiC hollow spheres resulted in a lower CTE.
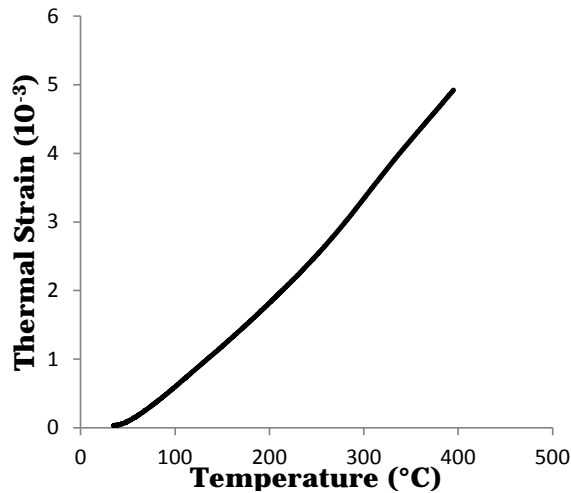
Fig. 49   Thermal strain-temperature response for a S1 syntactic foam specimen

Table 5   CTE values of the A356/SiC syntactic foams

Sample	CTE (100–200 °C) (µm/m °C)	CTE (300–400 °C) (µm/m °C)	Mean CTE (µm/m °C)
S1	11.67 ±0.42	16.35 ± 0.66	14.60 ± 0.91
S2	12.70 ±0.36	17.61 ± 0.40	15.74 ± 0.74

Although limited in scope, the results of this study suggest that the thermal properties of a syntactic foam can be determined, to a degree, by the nature of the hollow spheres used in their construction. Further studies are needed to fully quantify the influence of not only sphere composition, but also such properties as wall thickness and diameter.

4.4 Ballistic Impact Studies on Lightweight Metal Alloys for Armor

During the very early stages of the project, DST produced plates of AA5083 containing M350 maraging steel hollow spheres (Fig. 50) that were subjected to ballistic testing. At the time of this effort, DST was still developing and perfecting their production methods for both spheres and syntactic foams. Indeed, an examination of the as-processed plates prior to testing revealed that a significant percentage of the M350 spheres had actually been filled with the aluminum matrix during casting due to the presence of pores in the shell walls. Consequently, the performance of the plates was influenced by the filled spheres and the resulting ballistic results were not particularly noteworthy. That said, however, interesting observations were made during the subsequent microstructural analysis of the cross sections in terms of penetration, deformation of the maraging steel spheres, as well

as matrix-sphere adhesion/separation in the regions adjacent to the projectile/penetrator, as a function of projectile type and velocity.

Fig. 50   M350 maraging steel hollow spheres cast into an AA5083 matrix

The effect of penetration of 0.30-06-cal., 165-gr APM2 round for the case of impact through the sphere side (samples D1 and D2) and impact through the aluminum side (samples A1 and A3) is shown in Fig. 51. Impact through the aluminum side causes more damage from spall occurring along the opposite (lower) sphere side region, compared with when the impact is through the sphere side. In the latter case (impact through the sphere region), the opposite (lower) aluminum region is able to tolerate much higher tension through increased deflection. On the other hand, generation of spall in the sphere side region occurs relatively easily due to crack propagation through the sphere-matrix interfaces. Spall occurs because of tensile stresses formed due to wave reflection at the back free surface, resulting in removal (de-adhesion) of spheres from the surrounding matrix.
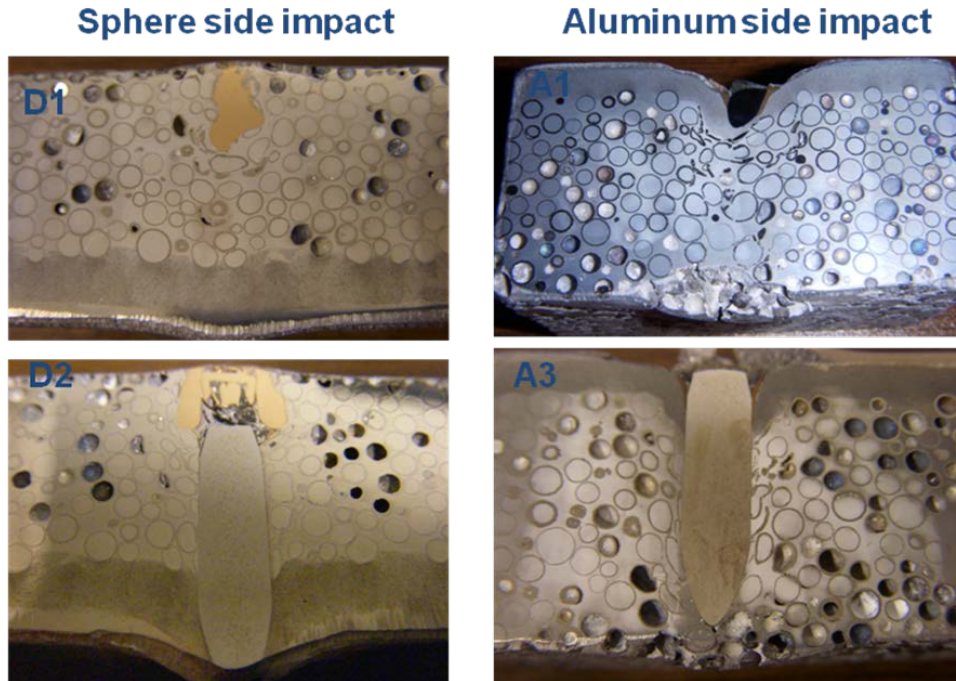
Fig. 51   Microstructures of cross sections of samples impacted with 7.62-mm APM2 round comparing effects of direction of impact through sphere side (samples D1 and D2) and aluminum side (samples A1 and A3)

A similar effect of increased damage during penetration of a 0.50-cal. fragment simulating projectile (FSP) projectile through the aluminum side is also observed with spall occurring relatively easily along the (opposite) sphere side of the sample. Figure 52 compares the effect of penetration in samples B1 and B3 at 2 slightly different velocities, with sample B3 showing slightly greater penetration depth and more obvious shear-induced failure ahead of the projectile. In general, while the filled spheres show deformation in the region ahead of and in the proximity of the projectile, the hollow spheres show more extensive deformation, spreading across a 45° fan. Pinching of hollow spheres as they are squeezed between other filled and unfilled spheres is also observed. Such large-scale deformation and pinching is indicative of significant energy dissipation. The bottom part of the composite in the sphere side region illustrates spall failure with removal (de-adhesion) of the spheres from the surrounding matrix.
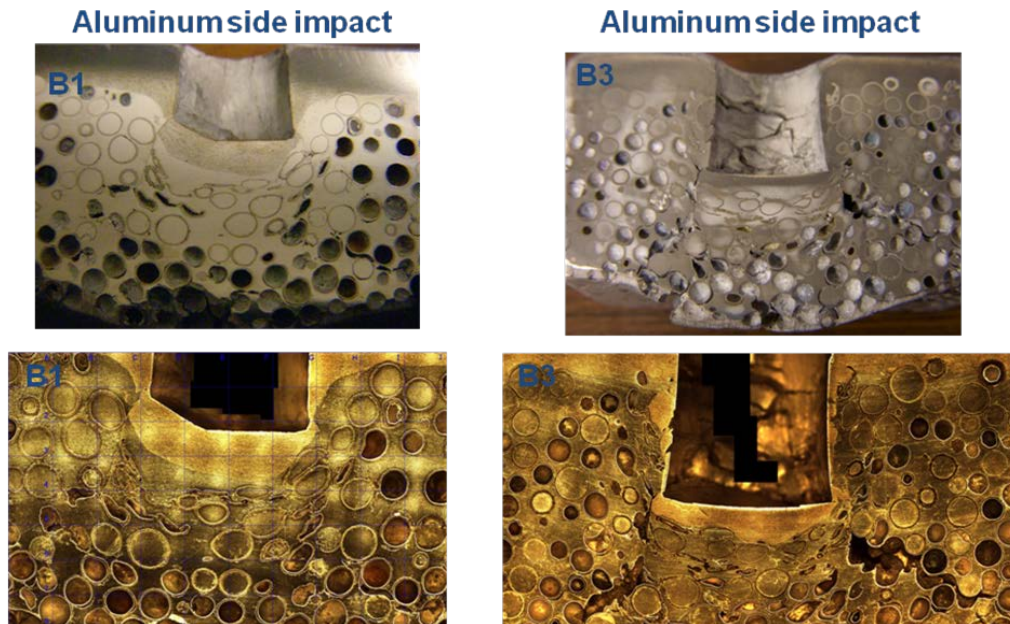
Fig. 52 Microstructures of cross sections of samples impacted with 50-cal. FSP round through the aluminum side at 2 slightly different velocities showing failure dominated by shear and spall along the sphere side

The overall ballistic performance of this syntactic foam sample is biased by the nonuniform characteristics of the maraging steel spheres being filled with the matrix material and not being present in the unfilled state. Nevertheless, it appears that the penetration through the aluminum side makes the sample weaker resulting in more damage via spallation and decohesion of the spheres from the matrix. Penetration through the sphere side appears to provide increased damage tolerance and resistance to spallation due to the ability of the monolithic matrix (aluminum) region to undergo deformation. The presence of such a monolithic matrix layer at the sample back surface region, therefore, may be essential in the design of hollow-sphere-filled composite materials.

In a series of additional experiments, a syntactic foam sample received in the form of a block of approximately 40-mm thickness was machined into cylindrical rod-shaped samples of 7.62-mm diameter and 40-mm length for performing Taylor rod-on-anvil impact tests. This test allows for determination of the average dynamic yield strength of the material based on altered geometry of the recovered impacted sample, the impact velocity, and sample density. Density measurements were also performed on these cylindrical samples using the geometric method and the Archimedes water immersion method, with the measured density values listed in Table 6. The values of geometric density (which assumes right circular cylinder)

differ from measured Archimedes density in which water filling the exposed spheres gives smaller volume. The geometric density is thus considered more representative.

Table 6   Measured geometric and Archimedes density

Taylor samples	Geometric density (g/cm³)	Archimedes density (g/cm³)
D1	2.61	3.07
D2	2.52	2.97
Average	2.61	2.98
Min	2.50	2.80
Max	2.70	3.11

The Taylor rod-on-anvil impact experiments were performed by impacting the rod-shaped samples against a rigid anvil at velocities of 100 and 200 m/s, using a 7.62-mm diameter single-stage gas gun. The IMACON 200 framing camera was used to record the transient deformation patterns. Figure 53 shows frames captured at 12, 18, and 28 μs following impact, illustrating deformation of the rod along the impact face. The impacted samples were also recovered following impact, and their altered deformation profile was recorded. Figure 54 shows examples of the rods before and after impact at 100 m/s. The impacted sample shows generally axially symmetric radial deformation profile.
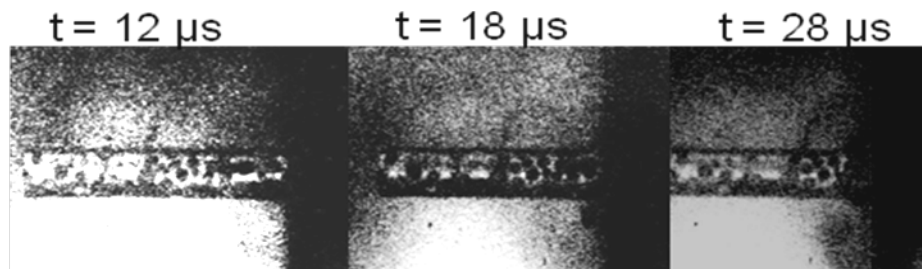
Fig. 53   High-speed camera images of transient deformation states captured at different times after impact
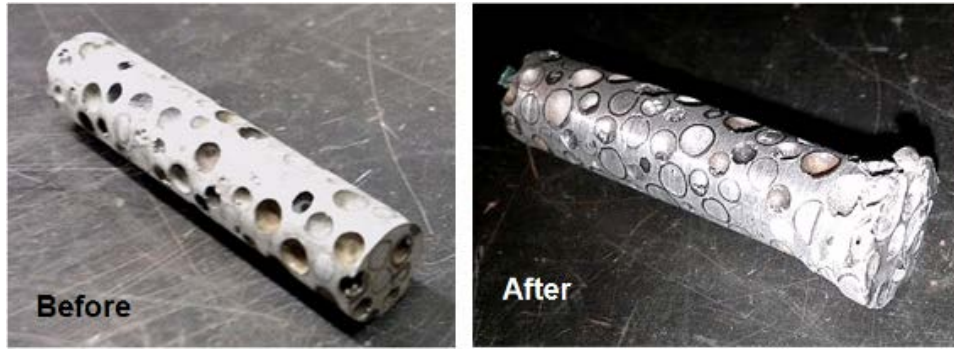
Fig. 54   Photographs of rod-shaped sample before and after impact at 100 m/s, showing generally axially symmetric deformation

The samples impacted at 200 m/s, however, exhibit asymmetrical radial deformation as illustrated in Fig. 55. The asymmetric radial deformation is not due to planarity of impact, but is a result of deformation region being influenced by a nonuniform distribution of filled and unfilled hollow spheres. Hence, the deformation becomes more skewed in areas containing a higher number of unfilled spheres. The nonuniform deformation, combined with large variations in sample density, made use of the Wilkins and Guinan method for determining the average dynamic yield strength quite difficult, with overall values that do not correlate with the extent of deformation. Hence, the method cannot be directly applied for such composite materials systems. What would be more beneficial is to employ mesoscale simulations that can be performed on 3-D microstructures obtained on actual samples and imported into the simulation scheme.
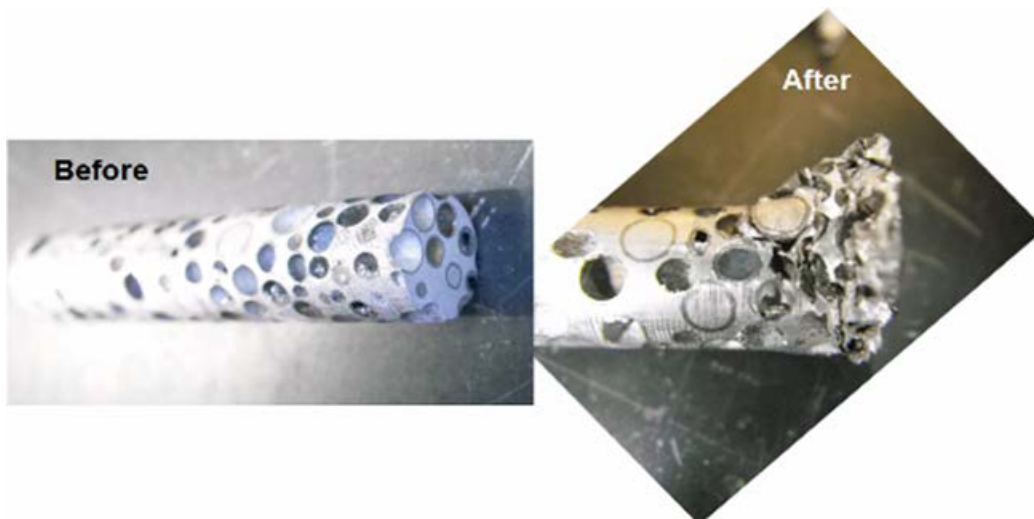
Fig. 55   Photographs of rod-shaped sample before and after impact at 200 m/s, showing axially asymmetric deformation of the rod due to nonuniform radial deformation along the impact region

The impacted samples were subsequently cross-sectioned and observed under an optical microscope to view the characteristics of deformation of the filled and unfilled spheres along the impact edge of the samples. The cross sections of the respective impacted samples at velocities of 100 and 200 m/s, are shown in Figs. 56 and 57. The Taylor rod-on-anvil impact tests provide a simple technique for determining the dynamic behavior of materials under compressive loading at high strain rates. The altered geometry of the impacted samples can be used to obtain a measure of the average dynamic yield strength corresponding to an average strain rate. However, the presence of maraging steel hollow spheres with varying distributions of filled spheres made it difficult to obtain a distinct value of the average dynamic compressive yield strength, due to asymmetric and non-uniform deformation patterns. Alternatively, it is possible to correlate the experimentally observed deformed profiles of the impacted samples (final and/or transient states) with those predicted employing numerical simulations. The correlation can then be used to generate and validate constitutive strength models for the material being investigated. The asymmetric and nonuniform deformation makes such a correlation difficult, unless the actual distribution of the filled and hollow spheres is accounted for. Hence, future work should involve generating 3-D images of the hollow-sphere-filled AMCs, and performing the simulations on actual realistic microstructures to capture the heterogeneity in the distribution of the filled and unfilled spheres. Nevertheless, it can be inferred from the results of the current Taylor rod-on-anvil tests that the asymmetric deformation pattern can in fact be beneficially used to preferentially propagate deformation in a certain direction, via appropriate arrangement of the distribution of filled and hollow spheres. Such a pattern of preferential flow could be of interest in the design of a system for armor application.
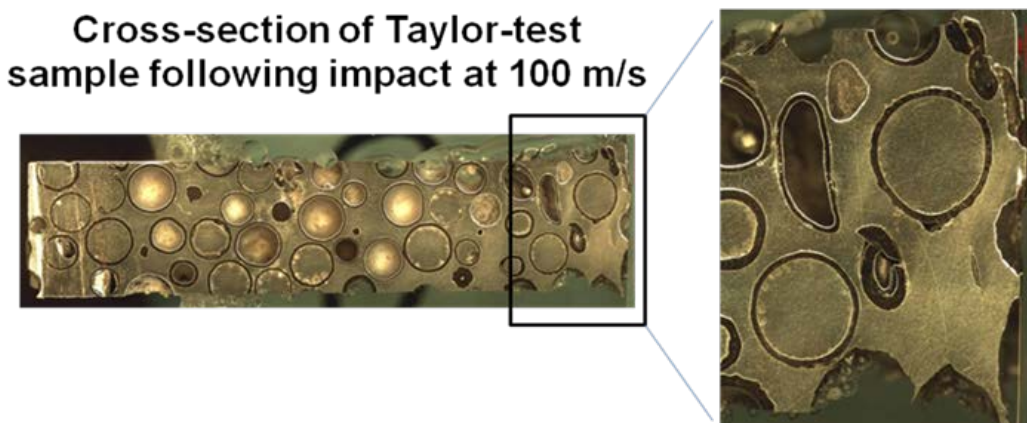
Fig. 56 Optical microstructure of cross section of rod-shaped sample after impact at 100 m/s, showing axially symmetric deformation of the rod and uniform deformation of the filled and hollow spheres
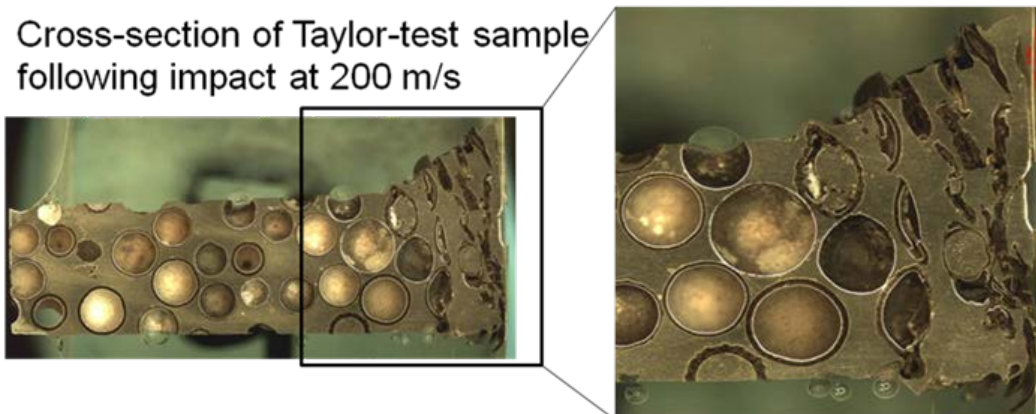
Fig. 57 Optical microstructure of cross section of rod-shaped sample after impact at 200 m/s, showing axially asymmetric deformation of the rod biased by the nonuniform deformation and distribution of the filled and hollow spheres

4.5 Ballistic Testing of LSAM Foams

Given the proven ability of the syntactic foams to absorb significant amounts of energy at quasi-static rates, it was decided to evaluate their performance under more extreme test conditions, specifically ballistic testing. The material system, test protocols, and results are presented in this section.

4.5.1 Material Design

As part of the material system design, it is important to realize that the metal foam is not a homogenous monolithic material; rather, the construction can be tailored to fit a specific threat or application. The information presented in this section is a brief overview of selected component materials (AA5083 matrix, SiC hollow spheres) and arrangement possibilities.

The metal foam densities for certain combinations have been determined through fabrication trials. The constituent materials densities are assumed to be 2.70 g/cm^3 for the aluminum matrix and 0.60 g/cm^3 for the SiC hollow sphere. The sphere density (true) can be adjusted from 0.24 g/cm^3 to over 2.0 g/cm^3 to meet design requirements.

The test panels will have 3 distinct layers—SiC tile strike face, LSAM layer, and an aluminum alloy backing layer—that will each have a range of thicknesses designed to produce a test panel with an areal density near 14.0 psf (Fig. 58). While it is possible to construct the foam composite without a backing layer, an initial series of tests indicated that a minimal layer of homogenous matrix material is advantageous to the performance of the LSAM system. The backing layer acted

as a stiffener to the LSAM layer, thereby allowing the spheres and matrix to absorb the energy as opposed to being pushed out by the projectile. The specific details for each layer are outlined as follows:

- SiC tile (Strike face). Five-millimeter-thick, 50-mm-square SiC tiles from Superior Graphite were used in the testing. These tiles were undermatched for the threat (0.30-cal. APM2). The gap between SiC tiles was held at 25 mm to eliminate tile-tile damage.

- Adhesive. A polysulfide adhesive was selected to attach the SiC tiles to the LSAM substrate. CS 3204 (type A) is a 2-part polysulfide base compound that cures at room temperature. Previous ballistic testing of SiC tiles bonded with CS3204 (type A) had indicated that this system provided acceptable performance. The SiC tiles remained attached to the LSAM test panel throughout the V_{50} test.

- LSAM and Integrated Backing. LSAM layers with the desired sphere content and integral backing layer were fabricated for incorporation into the armor package. As seen in Table 7, the thickness of the integral backing layer was sequentially reduced with a corresponding increase in the LSAM layer thickness. A picture of the final test assembly is shown in Fig. 59, with the actual areal densities for each panel given in Table 8.
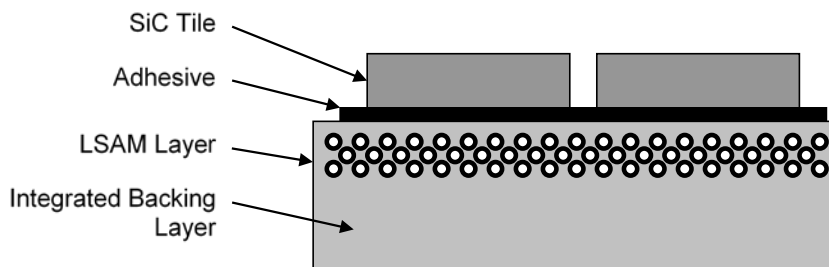
Fig. 58   LSAM test panel construction

Table 7   Test panel build schedule

Panels	SiC tile (mm)	LSAM (AA5083/SiC) (mm)	Backing (AA5083) (mm)	Total thickness (mm/inch)	Areal density SiC/LSAM/backing (psf)
1A, 1B	5.0	5.0	16.5	26.5/1.04	14.235
2A, 2B	5.0	10.0	13.0	28.0/1.10	14.184
3A, 3B	5.0	16.5	9.0	30.5/1.20	14.421
4A, 4B	5.0	20.0	6.5	31.5/1.24	14.358

Fig. 59   As-built test panel

Table 8   Test panel (as-built)

LSAM Panel	Thickness (mm/inch)	Length (inches)	Width (inches)	Weight (kg)	Areal Density (psf)	
					LSAM panel	w/5 mm SiC tile
1A	19.9/0.79	13.81	9.69	4.400	10.44	13.67
1B	19.8/0.78	13.50	9.50	4.425	10.95	14.18
2A	21.2/0.83	13.31	9.31	4.300	11.02	14.25
2B	21.0/0.83	13.88	9.56	4.595	10.99	14.22
3A	25.9/1.02	12.82	8.34	3.699	10.98	14.21
3B	25.2/0.99	12.64	8.45	3.686	10.96	14.19
4A	26.9/1.06	12.78	8.45	3.715	10.92	14.15
4B	26.9/1.06	12.80	8.43	3.684	10.84	14.07

4.5.2 Test Results

A series of panels, with and without the LSAM layer, were prepared for testing. A baseline panel (DOE Mil Spec Baseline) was fabricated from certified AA5083, MIL-DTL-46027K(MR) (2007) plate 0.75 inches (19.05 mm) thick (Clifton Steel, Maple Heights, Ohio) and 5.0-mm SiC tiles (Superior Graphite). The AA5083 thickness of 0.750 inches was selected because it was the closest thickness that would result in an areal density nearest to the LSAM test panels. The baseline panel (with SiC tiles) had an areal density of 13.76 psf. Next, a second all-aluminum

baseline panel (DOE 7B) was fabricated by the same pressure-casting method used to produce the LSAM panels. This panel was 100% aluminum and did not contain any hollow spheres. The panel measured $9 \times 13 \times 0.787$ inches ($228 \times 330 \times 20$ mm) and weighed 8.866 lb (3.925 kg) for an areal density of 10.80 psf. The panel was mounted with the same SiC 5-mm tiles bringing the total areal density to 14.03 psf. Finally, a series of LSAM panels were prepared according to the "recipe" listed in Table 8.

Ballistic testing was performed at Chesapeake Testing (Belcamp, Maryland) against a 0.30-cal. APM2 threat. The resulting 3×3 V_{50} values for each panel are shown in Fig. 60 as a function of areal density. As a quick reference the legend includes the layer thickness percentage for the LSAM and backing layers for each panel. For example, in the plate DOE 7B the layer ratio is (0/100) indicating 0% LSAM (hollow shells) and 100% backing (aluminum). For DOE 4B the ratio is 75% LSAM and 25% backing (aluminum).

As seen in the figure, the baseline panel (from Clifton Steel) had the highest V_{50} value at 2840 fps, followed by the panel produced via pressure casting. Interestingly enough, the highest V_{50} for the LSAM panels was obtained for panel DOE 4B, which had approximately 75% LSAM and 25% backing layer. The V_{50} values tended to decrease with increasing backing (solid metal) layer thickness.
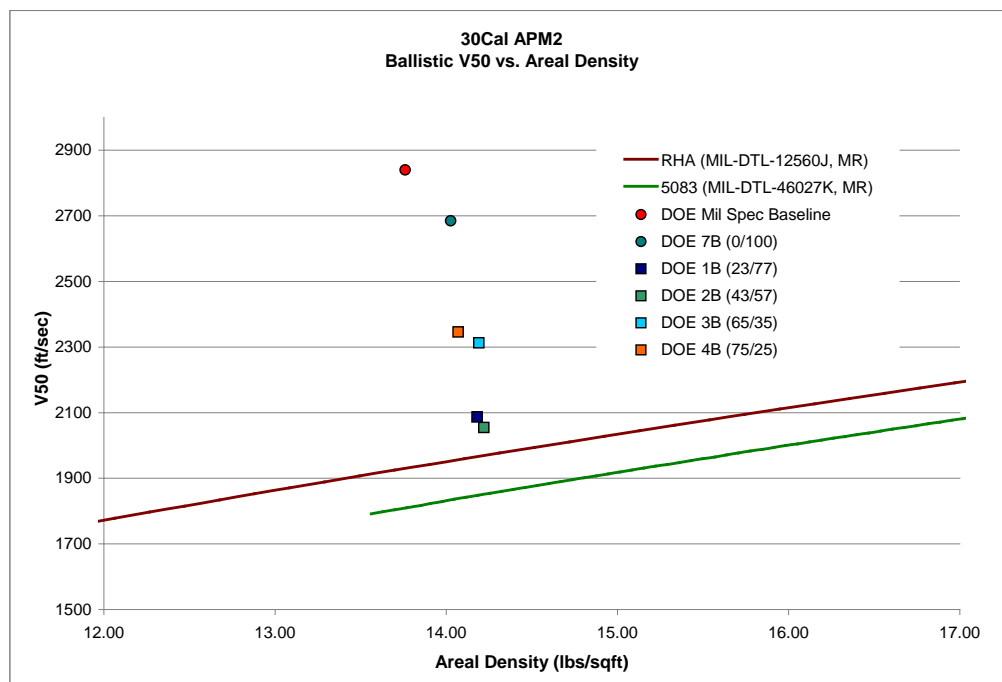
Fig. 60   Ballistic results

4.5.3 Prototype Armor Design

The results of the ballistic testing indicated that panels having a higher percentage of their thickness being the syntactic foam layer showed better ballistic response. Based on this observation, an armor system was fabricated that incorporated a LSAM panel with a minimum of a 70% syntactic foam layer thickness. This panel would be closest to test panel 4B. In addition, the system also included a 5.55-mm Kevlar backing panel, with the exact layup for the armor system given in Table 9.

Table 9   Armor system layer build

Description	Thickness	Density	Areal density
	mm	g/cm^3	lb/ft^2
SiC Tile (50 mm × 50 mm)	11.1	3.15	7.161
Adhesive (Sikaflex)	0.5	0.98	0.100
LSAM	10	2.25	4.608
AA5083	3	2.7	1.659
Adhesive (Sikaflex)	0.5	0.98	0.100
Kevlar panel	5.55	1	1.137
Total	30.65	. . .	14.766

This prototype armor system was tested in the same fashion as used for the earlier testing of the LSAM DOE panels. After a series of shots at increasing velocities, it was determined that the 0.30-cal. APM2 threat was unable to penetrate the panel and the testing was halted at 3712 fps.

Although the prototype armor system was successful from a ballistic perspective (3712 fps with no penetration), the armor system proved to have an areal density that was deemed too high. A review of the system construction identified the following factors:

1) The HMSC had a density of 2.25 g/cm^3.

2) The Sikaflex adhesive was applied very liberally to ensure bonding and added parasitic weight.

3) The rear aluminum backing layer was not consistent in thickness and may have added unnecessary weight.

In an effort to address these issues, a new panel design with the following improvements was prepared:

1) The density of the HMSC panels was reduced to 1.55 g/cm^3.

2) A thermoplastic polyurethane adhesive available in sheet form and recommended for ballistic layer bonding was used in panel construction. The use of the sheet adhesive minimized the amount of excess adhesive present in the panel.

3) The panels were prepared without a backing layer of aluminum.

As seen in Table 10, these modifications resulted in an approximate 30% reduction in the areal density of the test panels. In addition, appreciable cost savings were also achieved through the purchase of SiC tiles from Superior Graphite (Hopkinsville, Kentucky) rather than from BAE Systems ($0.98/in^2 vs. $9.50 /in^2, respectively).

Table 10 Description of the prototype armor system with a reduced areal density resulting from select layer modifications

Layer	Description	Thickness		Density	Areal density	
		inch	mm	g/cm^3	lb/ft^2	g/cm^2
1	SiC Tile (10 mm)	0.394	10	3.12	6.390	3.12
2	Adhesive	0.04	1	0.98	0.201	0.098
3	LSAM	0.39	10	1.55	3.175	1.55
	AA5083	0.00	0	2.7	0.000	0
4	Adhesive	0.04	1	0.98	0.201	0.098
5	Kevlar	0.04	1	1	0.205	0.1
	Total	0.904	23	. . .	10.172	4.966

The assembled panels were subsequently tested against the 0.30-cal. APM2 threat by Chesapeake Testing (Belcamp, Maryland), with a 3×3 V$_{50}$ of 2,675 fps reported. As constructed, the armor system described here provides similar levels of ballistic performance at a lower areal density than that recently published in the literature (Fig. 61) (Garcia-Avila et al. 2015). The 3 sets of data shown from the literature are for an approximately 30-cm test panel of B$_4$C strike face, a metal foam consisting of stainless steel hollow spheres in a steel matrix, and a backing plate of Kevlar (lowest areal density), aluminum (middle areal density), or no backing plate (highest areal density). Furthermore, it should be pointed out that the numbers shown for the literature report represent 2 shots and not an experimentally obtained ballistic limit (e.g., V$_{50}$).
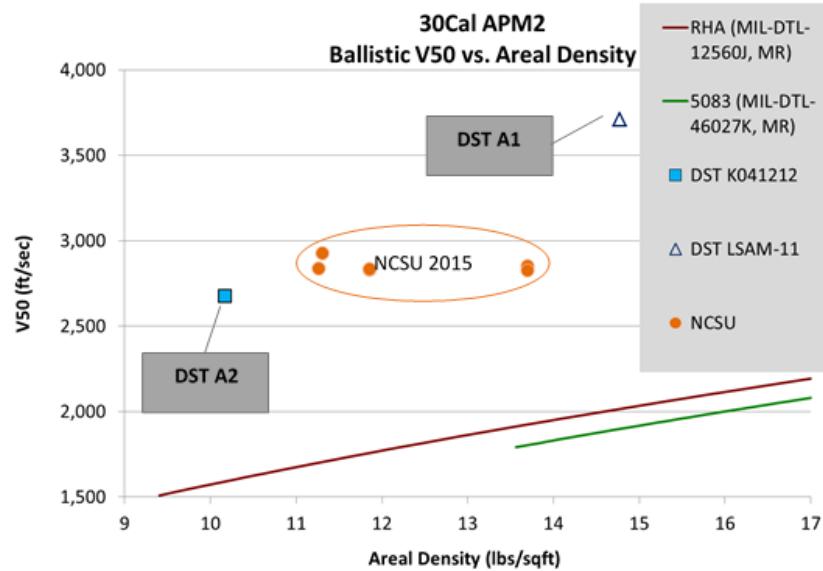
NCSU 2015 data adapted from Garcia-Avila M, Portanova M, Rabieia A. Ballistic performance of composite metal foams. Composite Structures. 2015;125:202–211.

Fig. 61   Ballistic test performance of composite metal foams relative to the minimum requirements for monolithic rolled homogeneous armor and AA5083.

4.5.4 Additional Ballistic Testing of AA5083 Alloy and AA5083 with SiC Hollow Spheres

A reverse ballistics experiment was performed on AA5083 alloy containing SiC hollow spheres. The Al-SiC hollow sphere composite was in the form of a 27-mm-thick section affixed to the front of a 127-mm-long, 80-mm-diameter aluminum sabot for reverse ballistic testing at 660 m/s. The Al sabot was machined with an 8-mm-wide step and 28-mm-deep pocket such that the diagonal edges of the composite slab (shown in Fig. 62 [left]) rest on the step and maintain an air gap to allow free travel of projectile into the Al sabot witness material. Figure 62 (right) shows the steel bullet-shaped target of 7.62-mm diameter and 31.78-mm length held in the center of the gun axis by a 6-mm piece of polymethyl methacrylate (PMMA).

Fig. 62 Composite slab mounted on Al sabot (left) and 7.62-mm steel bullet mounted on PMMA plate (right)

Following impact, the sabot and composite material were soft recovered in a catch tank of packed rags. The front of the aluminum sabot was removed by turning on a lathe and the sample was extracted. As illustrated in Fig. 63, the Al-SiC composite rear surface (far right image) did not show evidence of impacting the bottom of the pocket in the aluminum sabot. The steel bullet was captured in the aluminum sabot after it completely penetrated through the 28-mm-thick Al-SiC hollow-sphere composite slab and into the backing Al to a depth of 20 mm. The rear (Al-side) surface of the composite shows some radial cracking and some material removed near the hole, but no evidence of the composite material (spheres or Al matrix) impacting the sabot material.

Fig. 63 Images of recovered composite and sabot materials following reverse ballistic experiment at 660 m/s, showing clean penetration of the steel bullet through the Al-SiC composite and the travel of the bullet into the backing sabot material

Close observation of the recovered impacted sections revealed that there was practically no compression of the slab. The composite retained its original height of 27 mm in the central part that was unsupported by the aluminum sabot. The impact with the plastic target ring holding the bullet pressed the central section into the void space in the sabot while removing the material in the area supported by the sabot. The recovered Al-SiC hollow sphere composite was cross-sectioned to observe the penetration response more closely. A clean penetration of the composite was observed as illustrated in the cross sections of samples in Fig. 64.

Fig. 64   Cross section of Al-SiC composite penetrated by the 7.62-mm steel bullet at 660 m/s

An additional penetration test was performed on a 15-mm-thick AA5083 sample containing SiC hollow spheres. This experiment was performed using a 7.62-mm light gas gun with the bullet penetrating the aluminum target at approximately 364 m/s. A high-speed camera was used to observe the material during impact, as shown in Fig. 65. The bullet's axis is initially perpendicular to the sample face. The results reveal an interesting trend: upon impact, the trajectory of the bullet soon after penetration is altered. It is obvious that the presence of the SiC hollow spheres influences the bullet trajectory and reduces its efficiency for further penetration.
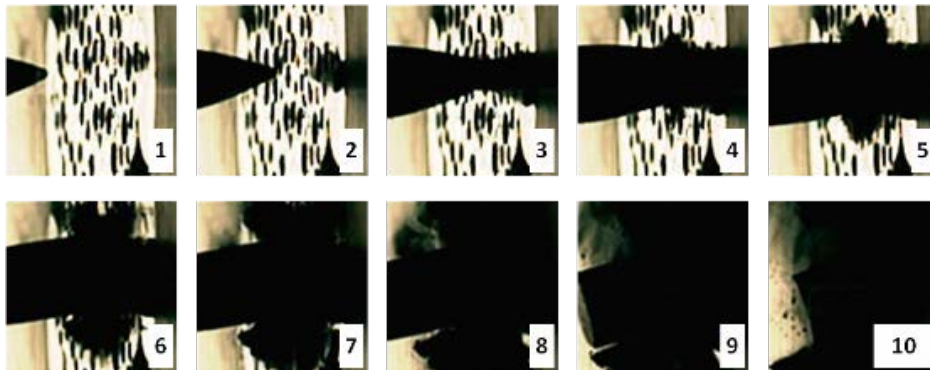
Fig. 65   High-speed images of a 0.30-cal. bullet impacting AA5083 with SiC hollow spheres at 364 m/s. The time lapse between each is 10 μs.

After testing, the sample was recovered for examination via SEM. The aluminum target was unable to stop the bullet for the chosen thickness. The target failed by cracking radially outward from the bullet. Cracking occurred preferentially at the aluminum-SiC interface, implying that increasing the interfacial strength is of interest for penetrating type impacts of this material. SEM images of the fracture surface of the recovered target are shown in Fig. 66. The interfacial nature of the cracking is apparent from the spherical holes visible in the fracture surface where the SiC hollow spheres previously resided. In Fig. 66a, a SiC sphere remains intact on the fracture surface. Figure 66b is a higher magnification image of a large interfacial crack inside one of the holes.

55
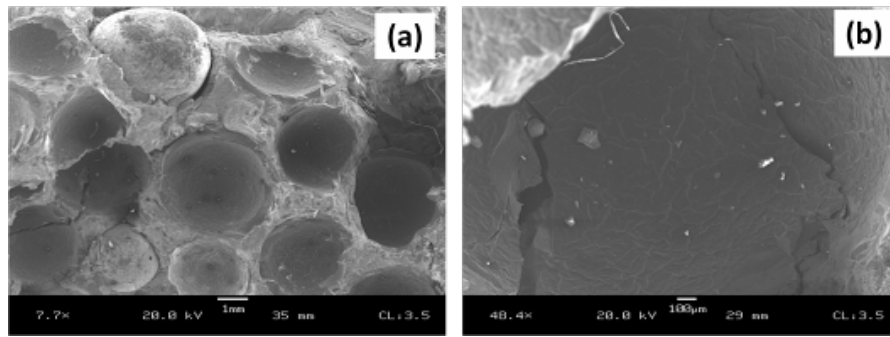
Fig. 66   SEM images of the fracture surface of the hollow sphere composite sample. The sample fails due to interfacial cracking after penetration by a 0.30-cal. bullet.

4.5.5 Impact Testing of Composite of Al with SiC Hollow Spheres

Plate impact testing was performed on the composite sample of Al containing SiC hollow spheres. Impact was performed with a 5-mm-thick AA5083 plate at 416 m/s using the 80-mm light gas gun. The impacted composite sample was soft recovered after impact, and it was observed that the material remained intact. The material thickness decreased from 14.9 to 11.3 mm after testing. The sample rear surface had an approximately 3-mm-thick aluminum layer devoid of SiC spheres. This layer was of similar thickness after testing implying that the reduction in thickness of the composite sample was due to the densification response of the sphere-impregnated layer.

The rear free surface velocity was measured via Velocity Interferometer System for Any Reflector (VISAR) during impact. It is observed that the rear free surface velocity never reached the expected measured velocity of the projectile even after 25 μs from the arrival of the first elastic wave. This result suggests that the composite target containing the SiC hollow spheres is serving as an effective target material for attenuating the shock waves from blast type impact events.

The velocity data were converted to a stress history diagram, and are plotted in Fig. 67. The data show several distinct features indicating the evolving shock compression and damage/failure mechanisms during impact. The inset in Fig. 67 shows a possible Hugoniot elastic limit (HEL), indicating the onset of plastic flow in the matrix. The HEL value was measured to be 0.22 GPa, which is of a similar magnitude to that seen previously for AA5083 H116. After the initial HEL, the stress increases up to 0.55 GPa followed by a sharp decrease. The stress then steadily rises up to approximately 0.90 GPa, where it reaches a plateau. At approximately 11 μs, the stress displays another sharp rise, after which the VISAR record loses resolution. The large increase in stress at long times is due to the air gap behind the flyer plate crushing and sending a secondary shock wave through

the material. If a larger air gap were chosen, then this feature may not be present in the VISAR data. The stress states captured by the VISAR trace, such as the first peak or the plateau stress, can provide indication of the "crush-strength" or stress at which the composite reaches full density following the collapse of the SiC hollow spheres, as these reveal indications of the damage response of the material. Computation of the crush-strength, however, needs correlation with model simulations.
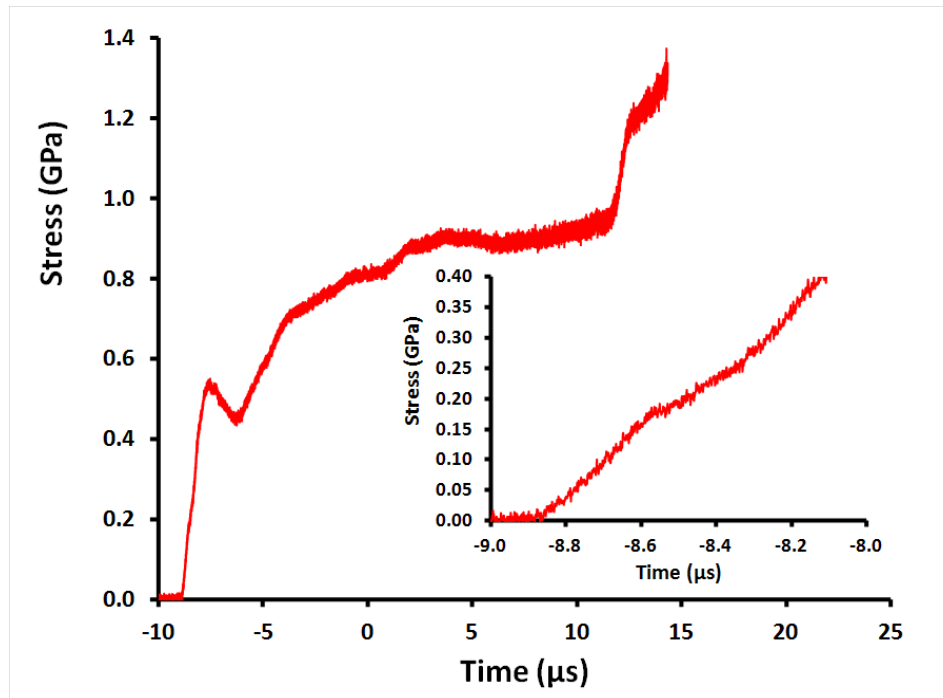
Fig. 67   **Stress history of AA5083 sample with SiC hollow spheres subjected to plate impact at 416 m/s**

The impact event corresponding to the previous experiment was simulated to ascertain the microstructural damage and failure mechanisms corresponding to the various stress features. Simulations were performed using the CTH 2-D multimaterial Eulerian hydrocode. The representative microstructure used for simulation was created from an image of the provided aluminum-SiC sample, with all other materials and geometries kept similar to the actual impact experiment. The simulated material response (Fig. 68) shows that the SiC spheres compress severely upon loading, at different states, until the composite reaches full density. The stress history corresponding to this type of compression response can be used to obtain information about the damage mechanism and overall shock-compression response of the composite. The simulated stress at the back surface of the sample is shown in Fig. 69. The same stress features are present in Fig. 69 as those that were observed in the VISAR data shown in Fig. 67 although the time scale in Fig. 69 is

shifted from that in Fig. 67. The simulated HEL and the first sharp decrease in stress occur at approximately 0.1 and 0.4 GPa, respectively, as opposed to the 0.22 and 0.55 GPa observed from VISAR results. Although the specific values from simulation are not identical to those seen in experiment since they are a function of the constitutive properties considered, the presence of the features is indicative of the actual material response during impact loading. This is an important result and can be used to compare different composite systems to determine the crush-strength not only as a function of the impact velocity but also the composite microstructure, including the matrix composition and phase characteristics and the volume fraction of the SiC hollows spheres (size, wall thickness, etc.) The crush-strength in turn can be related to the shock and blast attenuation properties of the composite material.
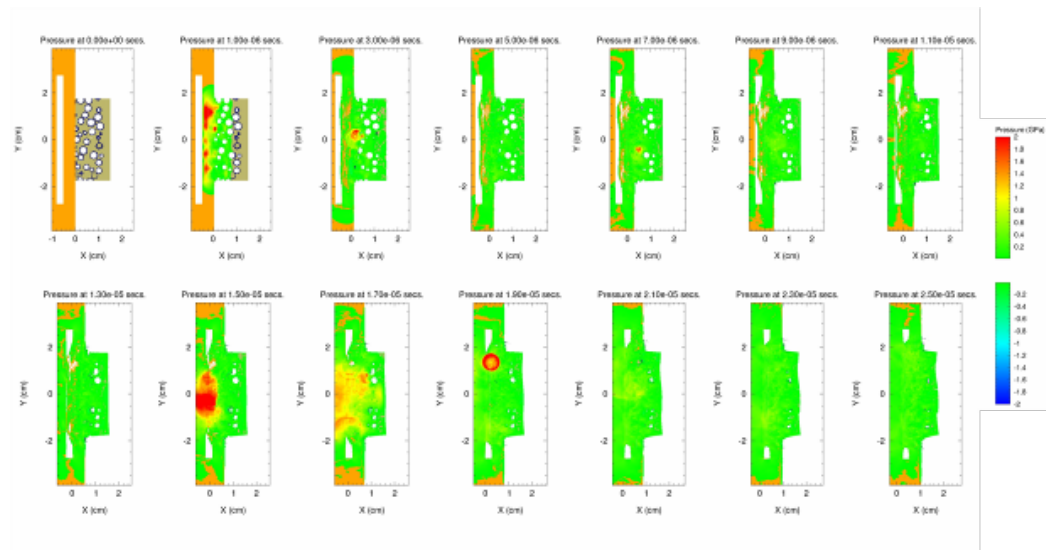
Fig. 68   Simulated material response of AA5083 sample with SiC hollow spheres subjected to plate impact at 416 m/s. The change in pressure with time throughout the material is also shown.
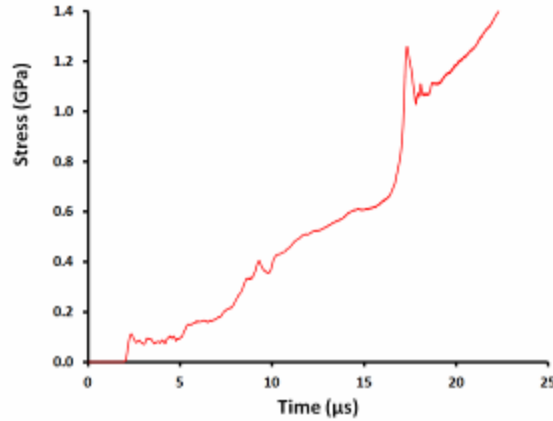
Fig. 69   Simulated stress history for a representative AA5083 sample with SiC hollow spheres subjected to plate impact at 416 m/s

4.6 Acoustic Impedance

In addition to the ballistic impact performance studied in Section 4.5.5, it can be expected that a LSAM plate could be part of an armor system exposed to blast loading conditions. Cost and time associated with large-scale blast event testing is not trivial and as a result armor designers often use a model based on acoustic impedance to predict the transmission and reflection of blast waves through materials. To determine the acoustic impendence of a material, both the density of the material and the speed of sound transmitted through the material are needed. The impedance is the product of the density and acoustic velocity as shown in Eq. 12.

$$Z = p * V, \tag{12}$$

where Z is impedance (kg/m^2-s), P is density (kg/m^3), and V is acoustic velocity (m/s).

For shock waves oriented normal to a planar surface having 2 layers of materials the predicted transmission is given as a ratio

$$R = \frac{2Z_2}{Z_1 + Z_2}, \tag{13}$$

where Z_1 is impedance of material 1, Z_2 is impedance of material 2, and R is the transmission ratio.

In an effort to obtain some insight into the potential behavior of LSAM plates, the acoustic impedance of A356 matrix syntactic foams formed with spheres of various ceramics was determined. The observed acoustic impedance properties were then

compared with properties of monolithic aluminum to determine the potential benefits of LSAMs.

4.6.1 Materials and Methods

The SiC hollow spheres used in the panels were manufactured by DST (Toledo, Ohio). Hollow spheres with diameters of 1 and 3 mm were used to construct test samples. Both the sphere wall thickness and fill content were varied to evaluate their influence on material performance. The A356 matrix syntactic foams were synthesized by the pressure infiltration method. Representative photographs of the A356/SiC foam material shown in Fig. 70 indicate that the spheres are well distributed in the material. Extensive postprocessing microscopy confirmed that the specimens did not have any measurable porosity.

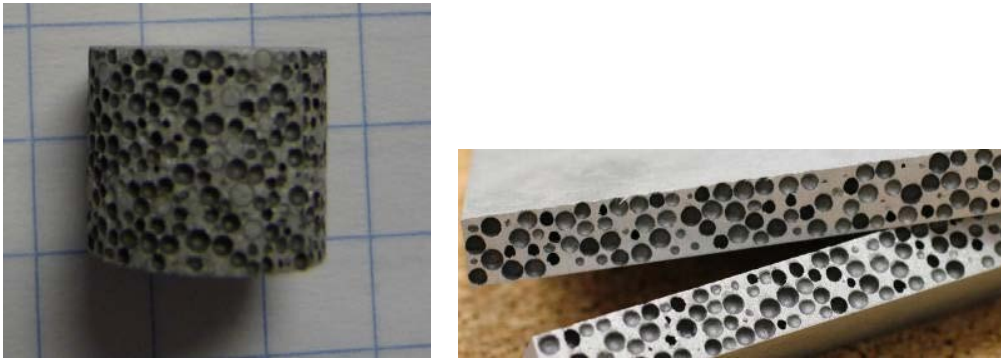**Fig. 70   A356 matrix syntactic foam with a) 1- and b) 3-mm SiC hollow spheres**

Panels were also made with 3-mm-diameter Al_2O_3 hollow spheres in which the shell density was varied in an effort to determine the influence of density on acoustic impedance. A photograph of an A356 panel cast with Al_2O_3 in Fig. 71 highlights the loose spheres and a cross-sectioned cut from a panel in the casting set.

Fig. 71   A356 matrix syntactic foam with 3-mm Al2O3 hollow spheres

A Physical Acoustics Ultrapac immersion type ultrasonic system and transducers were used to record the sound velocity for each sample. For the testing reported, a 20-MHz transducer was used. The system setup had both longitudinal and shear wave transducers. The acoustic impedance was determined from the density and measured acoustic velocity according to Eq. 12.

4.6.2   Results

The results for the various samples evaluated in this study are presented in Table 11. Prior to measuring the response of syntactic foams, an A356 aluminum plate was evaluated to establish the accuracy of the test system. The experimental value measured for the wave velocity was 6390 m/s, in very good agreement with the value of 6370 m/s that is commonly reported.

In regard to the LSAM samples, the data listed in Table 11 and illustrated in Fig. 72 clearly show a direct correlation between the acoustic impedance and the density of the syntactic foam; that is, as the density increases, typically so does the impedance. Furthermore, a comparison of impedance values for a density value of approximately 1.6 indicates that an Al_2O_3–containing foam would have the lowest impedance, followed by B_4C and then SiC. Thus, it clearly appears that the factors controlling the dampening properties of the syntactic foam are the average foam density and the sphere material.

Table 11 Acoustic impedance for the indicated samples

| Material	Wave speed (m/s)	Composite density (kg/m³)	Acoustic impedance [kg/(m²-s)]*10⁶
Aluminum (A356)	6,390	2,700	17.25
Magnesium (AZ91)	5,770	1,850	10.67
Al_2O_3	11,000	3,980	43.82
SiC	11,820	3,160	37.35
B_4C	13,880	2,520	34.98
A356/1-mm SiC	1,083	1,819	1.97
A356/3-mm SiC	1,125	1,620	1.82
A356/6.5-mm SiC	1,045	2,003	2.09
A356/3-mm Al_2O_3	574	1,620	0.93
A356/3-mm Al_2O_3	575	2,110	1.21
A356/3-mm Al_2O_3	553	2,750	1.52
A356/3-mm B_4C	670	1,560	1.05
AZ91/3-mm Al_2O_3	891	1,150	1.02
AZ91/3-mm SiC	895	1,100	0.98
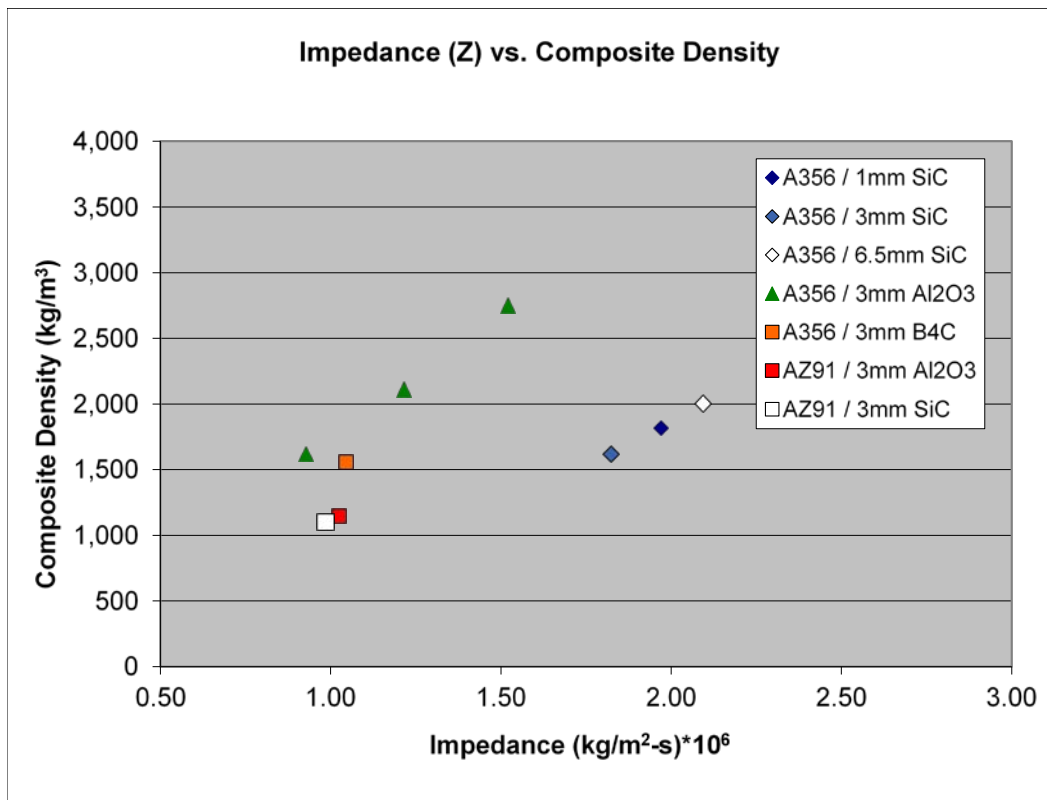
Fig. 72   Relationship between density and impedance for a number of syntactic foams

4.7 Welding Demonstration

The ability of a new material to be machined and joined by standard industrial practices is a critical factor in its potential use. Not surprisingly, early testing on syntactic foams showed that it could easily be machined by milling and/or water jet cutting to form panels with cutouts or mounting holes. However, it was unknown what effect the inclusion of the hollow ceramic spheres would have on the ability to weld the material.

In an effort to address this issue, DST evaluated the weldability of 2 aluminum-based syntactic foams. For the first case, syntactic panels consisting of 3-mm SiC hollow shells in A356 with a plate thickness of 10 mm were cut and welded to form a "T". Postwelding, the plates remained intensively hot for more than 45 min and had several voids at the surface exposing the SiC shells. Following this result, A356/Al_2O_3 hollow sphere syntactic panels with a thickness of 10 mm were cut and welded to form a "T" (Figs. 73 and 74). Both stick and continuous feed welding were attempted with the continuous wire feed being preferred. The weld was strong and broke at the plate and not the weld when struck, indicating deep penetration of the weld. Unlike the A356/SiC welding test, these panels were cool to the touch almost immediately after welding.
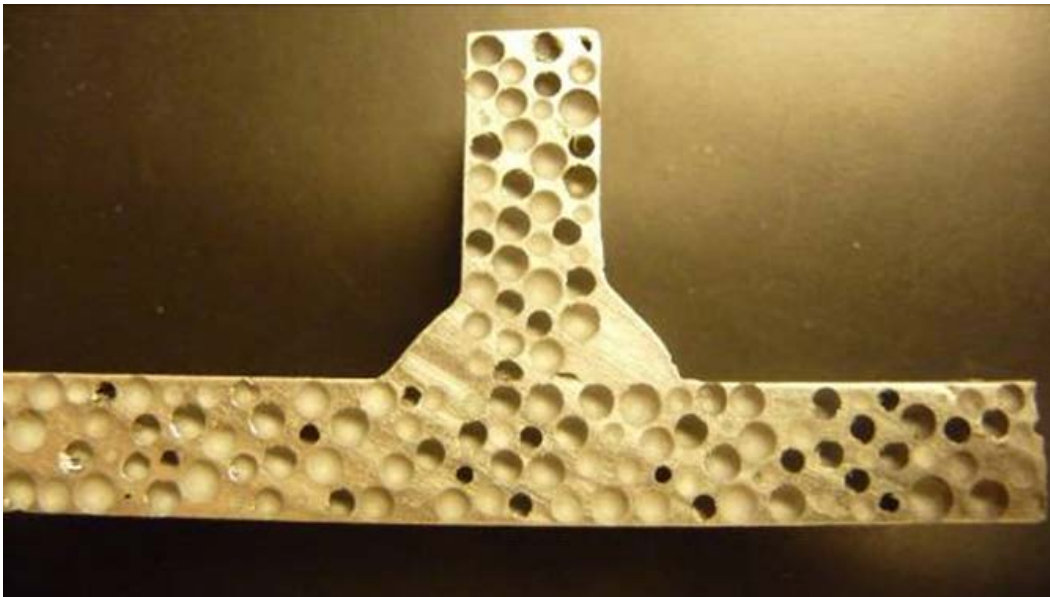

Fig. 73   Cross section: A356/Al_2O_3 welded panels

Fig. 74   Weld view: A356/Al₂O₃ welded panels

5.   Conclusions

Through the course of this project, DST has appreciably advanced the state of the art relative to the processing and characterization of hollow shells (e.g., spheres, prisms). In particular, the ability to produce high-quality shells in both metallic and ceramic compositions has been demonstrated. Furthermore, as a complement to this effort, a broad array of theoretical studies that yield insights into the mechanical response of hollow shells to applied loads has also been performed. The knowledge gained from such studies provided key insights into the subsequent use of the hollow shells in syntactic foams.

Initial efforts at producing metal matrix syntactic foams using a powder-based approach proved unsuccessful for a variety of reasons. Consequently, DST has developed relationships with proven metal casting shops that have given them the ability to produce syntactic foams in numerous alloys (e.g., Al-, Mg-, Fe-based) in sizes up to 1×1 m. The development of a stable hollow shell "preform" that served to prevent shell migration with the molten metal front was a key factor in their success. In addition, DST further improved their shell processing routine such that pores and/or microcracks in the shell wall were eliminated, thereby preventing the occurrence of metal-filled shells that was an issue in early casting efforts.

Once processing routines were established, the syntactic foams were subjected to a broad range of mechanical and physical testing. As expected, the foams offered significant weight savings as well as acceptable performance in numerous areas. Of particular note, the foams displayed a prolonged period of deformation and failure

under compressive loading that was free of strain rate sensitivity up to a strain rate of approximately 1500 s^{-1}. Although the foams did not display acceptable ballistic protection performance, an armor package that used the syntactic foam as a backing plate demonstrated the ability of such packages to provide the required level of ballistic protection at significantly reduced areal densities. Limited studies have also indicated that, depending on make-up, the foams could be easily welded to monolithic alloy plates as part of a larger structure. Finally, it should be noted that the results included in this report were not all-inclusive, but rather were intended to give insight into the potential applications of the syntactic foams.

As the Army continues to search for lightweight materials solutions, the hollow spheres and syntactic foams developed by DST provide viable options. As in all cases, there is the need to carefully select the shell and matrix composition to ensure that the resultant foam provides the required mechanical and physical performance. However, the combination of a broad array of shell compositions with the proven ability to encapsulate the shells in a metal matrix allows a large degree of flexibility in designing syntactic foams suitable for a given application.

6.   References

ASTM-D5004-11. Standard test method for real density of calcined petroleum coke by xylene displacement. West Conshohocken (PA): ASTM International; 2011.

Cox J, Luong DD, Shunmugasamy VC, Gupta N, Strbik O III, Cho K. Dynamic properties of hollow silicon carbide particle filled aluminum alloy A356 matrix syntactic foams. Metals. 2014;4:530–548.

Garcia-Avila M, Portanova M, Rabieia A. Ballistic performance of composite metal foams. Composite Structures. 2015;125:202–211.

Luong DD, Strbik O III, Hammond VH, Gupta N, Cho K. Development of high performance lightweight aluminum alloy/SiC hollow sphere syntactic foams and compressive characterization at quasi-static and high strain rates. Journal of Alloys and Compounds. 2013;550:412–422.

MIL-DTL-46027K(MR). Detail specification, armor plate, aluminum alloy, weldable 5083, 5456, and 5059. Aberdeen Proving Ground (MD): Army Research Laboratory (US); 2007 July 31.

Bibliography

Anantharaman H, Shunmugasamy VC, Strbik O III, Gupta N, Cho K. Dynamic properties of silicon carbide hollow particle filled magnesium alloy (AZ91D) matrix syntactic foams. International Journal of Impact Engineering. 2015;82: 14–24.

Gupta N, Luong DD, Cho K Magnesium matrix composite foams—density, mechanical properties, and applications. Metals. 2012;2:238–252.

Gupta N, Zeltmann SE, Shunmugasamy VC, Pinisetty D Applications of polymer matrix syntactic foams. JOM. 2014;66(2):245–254.

Labella M, Shunmugasamy VC, Strbik O, Gupta N. Compressive and thermal characterization of syntactic foams containing hollow silicon carbide particles with porous shell. Journal of Applied Polymer Science. 2014;131:40689.

Licitra L, Luong DD, Strbik O III, Gupta N Dynamic properties of alumina hollow particle filled aluminum alloy A356 matrix syntactic foams. Materials and Design. 2015;66B:504–515.

Macke A, Schultz A, Rohatgi PK, Gupta N. Metal matrix composites for automotive applications. In: Elmarakbi, A, editor. Advanced composite materials for automotive applications: structural integrity and crashworthiness. Hoboken (NJ): John Wiley and Sons, Inc; 2013 Dec.

Omar MY, Xiang C, Gupta N, Strbik O III, Cho K. Data characterizing compressive properties of Al/Al_2O_3 syntactic foam core metal matrix sandwich. Data in Brief. 2015;5:522–527.

Omar MY, Xiang C, Gupta N, Strbik O III, Cho K. Data characterizing flexural properties of Al/Al_2O_3 syntactic foam core metal matrix sandwich. Data in Brief. 2015;5:564–571.

Omar MY, Xiang C, Gupta N, Strbik O III, Cho K. Syntactic foam core metal matrix sandwich composite: Compressive properties and strain rate effects. Materials Science and Engineering. 2015;A643:156–168.

Omar MY, Xiang C, Gupta N, Strbik O III, Cho K. Syntactic foam core metal matrix sandwich composite under bending conditions. Materials and Design. 2015;86:536–544.

Rivero G, Schultz B, Ferguson J, Gupta N, Rohatgi P. Compressive properties of Al-A206/SiC and Mg-AZ91/SiC syntactic foams. Journal of Materials Research. 2013;28:2426–2435.

Shunmugasamy VC, Zeltmann SE, Gupta N, Strbik OM. Compressive characterization of single porous SiC hollow particles. JOM. 2014;(66):892–897.

Strbik OM. Hollow particles in metal matrix syntactic foams, edited by Gupta N, Rohatgi PK. 2014 June, DEStech, Lancaster PA.

List of Symbols, Abbreviations, and Acronyms

2-D   2-dimensional

3-D   3-dimensional

Al   aluminum

Al_2O_3 aluminum oxide

AMC   aluminum matrix composite

B_4C boron carbide

CTE   coefficient of thermal expansion

DMA   dynamic mechanical analyzer

DST   Deep Springs Technology

EDS   Energy dispersive X-ray spectroscopy

FSP   fragment simulating projectile

HEL   Hugoniot elastic limit

LSAM   Lightweight Syntactic Armor Material

Mg   magnesium

PMMA   polymethyl methacrylate

SEM   scanning electron micrograph

SHPB   split-Hopkinson pressure bar

SiC   silicon carbide

VISAR   Velocity Interferometer System for Any Reflector

1 (PDF)	DEFENSE TECHNICAL INFORMATION CTR DTIC OCA
2 (PDF)	DIRECTOR US ARMY RESEARCH LAB RDRL CIO L IMAL HRA MAIL & RECORDS MGMT
1 (PDF)	GOVT PRINTG OFC A MALHOTRA
1 (PDF)	DEEP SPRINGS TECHNOLOGY O STRBIK III
1 (PDF)	DIR USARL RDRL WMM F V HAMMOND